

**APPLICATION OF POSITRON ANNIHILATION  
SPECTROSCOPY TO THE STUDY OF DEFECTS IN  
PEROVSKITE TYPE MATERIALS**

**By**

**DMYTRO GREBENNIKOV, Specialist**

A Thesis

Submitted to the School of Graduate Studies

in partial Fulfillment of the Requirements

for the Degree

Master of Applied Science

McMaster University

© Copyright by Dmytro Grebennikov, April 2007

# Master of Applied Science (2007)

## (Engineering Physics)

McMaster University  
Hamilton, Ontario

TITLE	Application of Positron Annihilation Spectroscopy to the Study of Defects in Perovskite Type Materials
AUTHOR	Dmytro Grebennikov, Specialist
SUPERVISOR	Dr. Peter Mascher
NUMBER OF PAGES	x, 101

## Abstract

Formation of defects in ceramics  $BaA_{1/3}Nb_{2/3}O_3$  (where A=Mg,Co or Zn) suitable for microwave applications was analyzed by using positron annihilation spectroscopy and X-ray diffraction techniques. The dependence of the microwave properties of perovskite ceramics on the defect structure of  $ANb_2O_6$  (A = Mg, Co or Zn) that was used as a precursor during the sintering process prompted us to conduct positron analysis of  $ANb_2O_6$  columbites as well.

Positron lifetime experiments revealed only one defect type - grain boundaries- and demonstrated that the lifetime component originating from the annihilation in defects depends on the size of the grains contained in the materials. For perovskite samples where the grain sizes are smaller than those of columbite materials, the intensity of the defects' component is larger and varies within 28-40%. Results of coincidence Doppler broadening measurements confirmed the presence of only one type of defect in both materials, i.e. grain boundaries.

Theoretical calculations for the  $ANb_2O_6$  columbite system resulted in bulk lifetimes of  $\tau_b = 177, 176$ , and  $172 \text{ psec}$ , respectively for magnesium, zinc and cobalt columbites and are in agreement with experimental values. The presence of second phases in nonstoichiometric  $A_{1+x}Nb_2O_6$  (A=Mg,Co, or Zn) columbites did not change the bulk lifetimes of the columbite material because of the small difference in bulk lifetimes of the host material and impurities.

Ordering in perovskite type materials that influences the microwave properties in ceramics also changes the positron characteristics of perovskites. Theoretical simulations demonstrated that for the disordered cubic phase,  $\tau_b \approx 190 \text{ psec}$  and for

the completely ordered hexagonal phase,  $\tau_b \approx 240 p$  sec. The bulk lifetime of the final perovskite material greatly depends on the presence of the second phases (Ba-rich and, possibly, Co-rich) as well as on the fractional part of the hexagonal phase. The influence of additional phases on  $\tau_b$  is more significant than that of the “disordered-ordered” transition and can be used to monitor changes in the concentration of the former ones.

## Acknowledgments

First of all I want to express my thanks to Dr. Peter Mascher for his guidance and invaluable advice throughout the course of this work. His international collaborations let me meet new people in the field of my research. In particular, cooperation with the group of Dr. Belous (V.I.Vernadskii Institute of General & Inorganic Chemistry, Kyiv, Ukraine) through a NATO Science for Peace project let me obtain samples that I used in the present work.

Frequent discussions with Mr.Gong (Department of Chemistry, McMaster University) in the sphere of material preparation techniques helped me understand chemical aspects of my work. Priceless expertise of Dr. Simpson (University of Western Ontario, London) in technical details of the coincidence Doppler broadening setup whom I am also indebted was very useful for me.

Interpretation of the experimental results relies on the theoretical calculations. I am very thankful to Dr. Nieminen and his group from Helsinki University of Technology, Finland for their help in the calculation of theoretical values for the studied systems.

And of course, I am very appreciative to McMaster University, especially to the Department of Engineering Physics, for the financial assistance through teaching assistantship and departmental scholarship.

# Table of Contents

Chapter 1:	<b>Introduction</b>	1
Chapter 2:	<b>Microwave Ceramics</b>	4
	2.1 Review of Microwave Ceramics	4
	2.2 Perovskite Structure ( $ABO_3$ )	8
	2.3 Dependence of Temperature Coefficient of the Dielectric Constant on the Structure of the Material	10
	2.4 Origin of the Dielectric Losses	13
	2.5 Niobium vs Tantalum Based Perovskites	14
	2.6 X-ray Diffraction: Magnesium Niobate Perovskites as an Example of Disordered-Ordered Transition	16
Chapter 3	<b>Positron Annihilation Spectroscopy</b>	19
	3.1 Basics of Positron Annihilation Spectroscopy	19
	3.2 Source of Positrons	20
	3.3 Positron-Matter Interaction	21
	3.4 Diffusion of Positrons	23
	3.5 Trapping Model and Its Connection to the Experiment	25
	3.6 Theoretical Background	29
	3.6.1 Local Density Approximation (LDA)	29
	3.6.2 Generalized Gradient Approximation (GGA)	32
	3.6.3 Enhancement Factor	33
	3.7 Doppler Broadening Technique	35
	3.8 Brief Introduction to the Results of Positron Lifetime Spectroscopy for Perovskite Materials	38
	3.9 Positron Annihilation at Grain Boundaries	41
Chapter 4	<b>Description of the Samples</b>	44
	4.1 Columbite Samples	45
	4.1.1 Magnesium Columbite	45
	4.1.2 Cobalt Columbite	47
	4.1.3 Zinc Columbite	48
	4.2 Materials with Perovskite Structure	51

4.2.1 Cobalt Perovskite ( $Ba_3Co_{1+x}Nb_2O_9$ )	<b>51</b>
4.2.2 Cobalt Perovskite ( $Ba_{3+3x}CoNb_2O_9$ )	<b>52</b>
4.2.3 Zinc Perovskite ( $Ba_3Zn_{1+x}Nb_2O_9$ )	<b>53</b>
4.2.4 Zinc Perovskite ( $Ba_{3+3x}ZnNb_2O_9$ )	<b>54</b>
4.2.5 Magnesium Perovskites	<b>55</b>
<b>Chapter 5      Positron Annihilation Experimental Setup</b>	<b>56</b>
5.1 Lifetime Spectroscopy	<b>56</b>
5.2 Interpretation of Lifetime Spectra	<b>58</b>
5.3 Doppler Broadening Spectroscopy	<b>59</b>
5.4 S and W Parameters	<b>61</b>
<b>Chapter 6      Experimental Results and Their Discussion</b>	<b>64</b>
6.1 Columbite Materials	<b>64</b>
6.2 Positron Annihilation Spectroscopy of Perovskite Samples	<b>78</b>
6.2.1 $Ba_3MgNb_2O_9$ Sample	<b>80</b>
6.2.2 $Ba_{3+3x}CoNb_2O_9$ Samples	<b>83</b>
6.2.3 $Ba_3Co_{1+x}Nb_2O_9$ Samples	<b>86</b>
6.2.4 $Ba_{3+3x}ZnNb_2O_9$ vs $Ba_3Zn_{1+x}Nb_2O_9$ Samples	<b>88</b>
6.2.5 Defects in Perovskite materials	<b>90</b>
<b>Chapter 7      Conclusions and Suggestions for Future Work</b>	<b>93</b>
References	<b>95</b>

## List of Figures/Tables

Figure 2.1	Dependence of the temperature coefficient of the dielectric constant on the value of the dielectric constant for a number of materials	5
Figure 2.2	Perovskite type structure	8
Figure 2.3	Dependence of the temperature coefficient of the dielectric constant the on tolerance factor for some Ba and Sr-based perovskites	12
Figure 2.4	X-ray diffraction pattern for cubic phase of $BaMg_{1/3}Nb_{2/3}O_3$	17
Figure 2.5	X-ray diffraction pattern for hexagonal phase of $BaMg_{1/3}Nb_{2/3}O_3$	17
Figure 3.1	The decay scheme of the radioactive isotope of sodium-22	20
Figure 3.2	Emission spectrum of sodium-22	22
Figure 3.3	Scheme of the trapping model with one defect type	26
Figure 3.4	Lifetime versus density parameter	34
Figure 3.5	Comparison of Doppler broadened annihilation line for defect free sample and sample containing defects	36
Figure 3.6	Results of Monte-Carlo simulations for fraction of positrons (FPS) reaching grain boundaries versus diameter of the grains	42
Figure 4.1	Dependence of the quality factor in $Mg_{1-x}Nb_2O_6$ on the x value	46
Figure 4.2	Dependence of the quality factor in $Co_{1-x}Nb_2O_6$ on the x value	48
Figure 4.3	Dependence of the quality factor in $Zn_{1-x}Nb_2O_6$ on the x value	49
Figure 5.1	Positron Lifetime Experimental Setup	57
Figure 5.2	Coincidence Doppler Broadening Setup	60
Figure 5.3	Experimental Doppler broadened Annihilation Line	62

Figure 6.1	Dependence of the first lifetime component, $\tau_1$ , on the x value	<b>65</b>
Figure 6.2	Positron density distribution in columbite type materials	<b>69</b>
Figure 6.3	Results of reflection microscopy measurements	<b>71</b>
Figure 6.4	Dependence of bulk lifetimes in $A_{1+x}Nb_2O_6$ columbites on x value	<b>74</b>
Figure 6.5	Dependence of trapping coefficient on x value for columbite type materials	<b>77</b>
Figure 6.6	SW-plot for columbite type materials	<b>78</b>
Figure 6.7	Grained surface of perovskite type material	<b>79</b>
Figure 6.8	X-ray diffraction spectrum for a magnesium niobium perovskite sample	<b>82</b>
Figure 6.9	Dependence of $\tau_b$ on the $1+x$ value for $Ba_{3+3x}CoNb_2O_9$	<b>84</b>
Figure 6.10	X-ray diffraction spectrum for a cobalt niobium perovskite sample	<b>84</b>
Figure 6.11	Dependence of $\tau_b$ on $1+x$ value for $Ba_3Co_{1+x}Nb_2O_9$	<b>86</b>
Figure 6.12	Dependence of $\tau_b$ on $1+x$ value for $Ba_{3+3x}ZnNb_2O_9$ perovskite	<b>89</b>
Figure 6.13	Dependence of $\tau_b$ on $1+x$ value for $Ba_3Zn_{1+x}Nb_2O_9$ perovskite	<b>89</b>
Figure 6.14	S vs W curve for perovskite materials	<b>91</b>
Table 2.1	Examples of some dielectric materials currently used in industry as well as measured quality factors	<b>6</b>
Table 2.2	List of acronyms used in fig. 2.3	<b>12</b>
Table 3.1	Results of bulk and defect lifetime calculations in some $ABO_3$ perovskite type materials	<b>38</b>
Table 4.1	Results of X-ray and microwave measurements on	

$Ba_3Co_{1+x}Nb_2O_9$ perovskites	<b>51</b>
Table 4.2 Results of X-ray and microwave measurements on $Ba_{3+3x}CoNb_2O_9$ perovskites	<b>52</b>
Table 4.3 Results of X-ray and microwave measurements on $Ba_3Zn_{1+x}Nb_2O_9$ perovskites	<b>53</b>
Table 4.4 Results of X-ray and microwave measurements on $Ba_{3+3x}ZnNb_2O_9$ perovskites	<b>54</b>
Table 6.1 Decomposed components for stoichiometrical columbites	<b>66</b>
Table 6.2 Results of theoretical calculations of the bulk and defect lifetimes in columbite type materials by using Boronski-Nieminen enhancement factors within the Linear Density Approximation (LDA) and Arponen-Pajanne enhancement factors within the Generalized Gradient Approximation (GGA)	<b>67</b>
Table 6.3 Theoretical bulk and defects lifetimes for $BaA_{1/3}Nb_{2/3}O_3$ (A=Mg,Co or Zn)	<b>91</b>

# **Chapter 1**

## **Introduction**

The success of today's electronics depends on the ability to produce smaller and cheaper components. Progress made in the industry of semiconductors and ceramics resulted in the miniaturization and integration of microwave components [1].

Production of low-loss and temperature-stable dielectric resonators plays an important role in the development of filters, oscillators and antennas used for wireless communication. The major advantage of utilizing dielectric resonators is the reduction of their size based on the dependence of the resonance frequency on the dielectric constant of the media (the size of the resonator is inversely proportional to the square root of the dielectric constant)[2]. An application in the communications industry requires a material to have the following properties [3]:

- high quality (Q) factor and low losses
- stable and near zero temperature coefficient of resonance frequency
- relatively high dielectric constant ( $\epsilon_r$ )

There are several physical principles that put limitations on dielectric materials. The first constraint is based on the fact that the communication wavelength range is finite and the number of consumers is increasing. In order to provide satisfactory service for each customer, the producer of microwave components should guarantee that signals between neighboring bands would not intermix. Thus, creation of low-noise and narrow-band components would increase the capacity of the network

and by reducing losses in the components one could decrease the power supplied to the system (and, hence, its size).

The next requirement is established again by consumers wishing to operate equipment under different weather conditions: versatility of today's apparatus implies that it can operate under environmental temperatures varying in a wide range (usually from  $-20^{\circ}\text{C}$  and up to  $+80^{\circ}\text{C}$ ). To achieve this, the resonance frequency ( $f_{res}$ ) of the dielectric resonator should not change within the practical temperature range. The parameter used to characterize changes of  $f_{res}$  is called the temperature coefficient of the resonance frequency ( $\tau_f$ ) and its value should be reproducible and adjusted with an accuracy of 0.5-1 ppm/K near zero.

Finally, the necessity to use materials with relatively high dielectric constant is based on the fact that the size of the microwave resonator is inversely proportional to  $\sqrt{\epsilon_r}$ . Hence, by taking advantage of a high dielectric constant one can significantly minimize the size of the resonator.

In spite of the simplicity of the formulated requirements, there are a limited number of materials for which all three conditions (i.e. high Q-factor (low losses), near zero temperature coefficient of resonance frequency (TCF), and high  $\epsilon_r$ ) are satisfied simultaneously: large numbers of materials with high dielectric constant have either very low quality factor or TCF far from zero value. Thus, the successful search for a new material incorporating all three requirements would be advantageous for today's industry.

This work deals with the application of positron annihilation spectroscopy to the study of the process of formation of dielectric materials suitable for microwave applications and is organized as follows.

Chapter 2 contains a review of materials used in microwave applications so far and factors influencing their characteristics. Chapter 3 is devoted to the basics of the positron measurement technique and describes the main processes after positrons' penetration in the material. Theoretical background for positron lifetime spectroscopy provides a connection between the experimental output parameters of positron lifetime spectroscopy and those used to characterize dielectric resonators. Chapter 4 gives details on the sample preparation and shows results of X-ray and microwave measurements conducted at V.I.Vernadskii Institute of General & Inorganic Chemistry,NASU (Kyiv, Ukraine), from which all the samples used in this work were obtained.

Chapter 5 concentrates on the description of the experimental setup (namely positron lifetime and coincidence Doppler broadening setups) used for the positron measurements. Discussion of the experimental results and their connection to the theoretical calculations are given in the sixth chapter of this thesis. Chapter 7 provides conclusions and suggestions for future work.

## Chapter 2

### Microwave Ceramics

#### 2.1 Review of Microwave Ceramics

As was mentioned in the Introduction, the temperature coefficient of the resonance frequency should be near zero and not change significantly over practical temperature ranges. In general, changes in TCF occur because of the thermal expansion of materials and changes of the dielectric constant with temperature:

$$\tau_f = -\frac{1}{2}\tau_e - \alpha_i \quad (2.1)$$

where  $\alpha_i$  is the linear thermal expansion coefficient and  $\tau_e$  is the temperature coefficient of the dielectric constant ( $TC\epsilon$ ). Linear thermal expansion arises because of the anharmonicity of the lattice vibrations. Usually  $\alpha_i$  is on the order of 8–15 ppm/K. To compensate for changes in the linear size of media, materials with negative values of  $\tau_e$  ( $-15 \text{ ppm}/K < \tau_e < -5 \text{ ppm}/K$ ) have to be used [4].

Wolfram Wersing [2] collected experimental results on the dependence of the temperature coefficient of the dielectric constant on the value of the dielectric constant itself for a number of materials. His results are presented in fig.2.1. The first group of compounds having near zero  $TC\epsilon$  belongs to the ionic and covalent inorganic materials. Unfortunately rather low dielectric permittivities make them unsuitable for applications at microwave wavelengths. At the same time, paraelectric and ferroelectric materials have reasonably high dielectric constant ( $\epsilon_r = 60 – 100$ ) but the temperature coefficient of the dielectric constant has negative values that are

far from zero. In order to find a compromise between the temperature stability requirements and the size of the final product, several techniques have been developed [5-10]. For example, by mixing materials with different signs of  $\tau_\epsilon$ , it is possible to obtain dielectrics having high  $\mathcal{E}_r$  with reasonably low losses and near zero  $\tau_\epsilon$  [11].

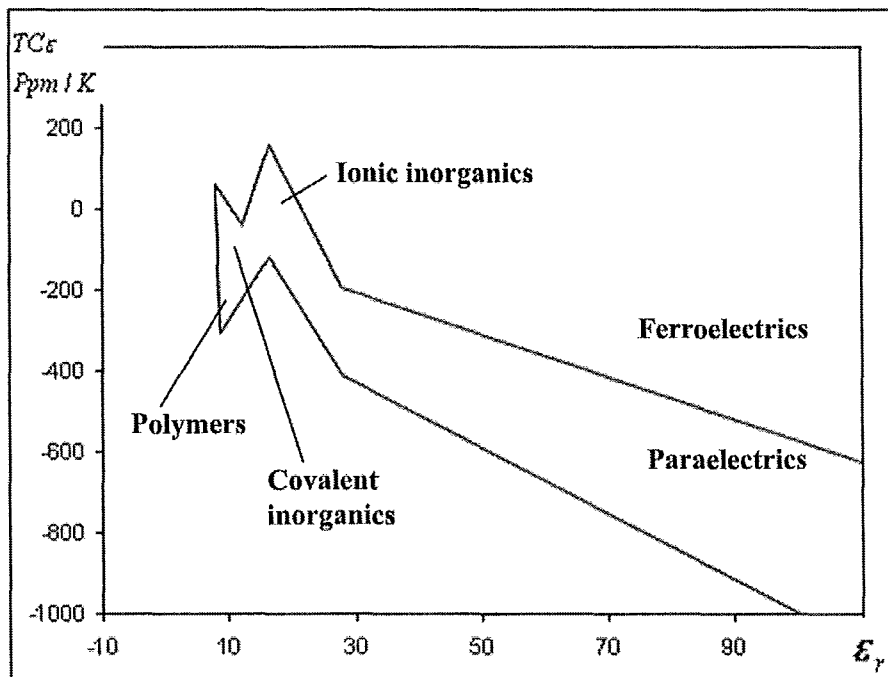


Fig.2.1 Dependence of the temperature coefficient of the dielectric constant on the value of the dielectric constant for a number of materials

Presently, there are several groups of ceramics that are widely used in industrial applications. Examples are listed in Table 2.1.

Barium titanates were the first dielectric materials having relatively high  $\mathcal{E}_r$ , that fulfilled all requirements and found practical application in microwave

Table 2.1 Examples of some dielectric materials currently used in industry as well as measured quality factors

Material	$\epsilon_r$	Q
$MgTiO_3$	21	8000
$Ba(Mg,Ta)O_3$	24	43000
$Ba(Zn,Ta)O_3$	30	14000
$(Zr,Sn)TiO_4$	38	10300
$Ba_2Ti_9O_{20}$	36	10700
$BaO \bullet Sm_2O_3 \bullet TiO_2$	80	3700
$BaO \bullet Nd_2O_3 \bullet TiO_2$	86	3000

electronics [12,13]. Among them were  $BaTi_4O_9$  and  $Ba_2Ti_9O_{20}$  both having almost identical relative dielectric constants and quality factors ( $\epsilon_r = 36$  and Q=10,000) but different TCF ( $\tau_f = 15 \text{ ppm/K}$  versus  $\tau_f = 4 \text{ ppm/K}$ , respectively) [14,15]. As was mentioned before, the simplest way to change  $\tau_f$  is to mix in a compound with the opposite sign of TCF. It turned out [16] that addition of  $ZnO$ ,  $SeO_2$  or  $Ta_2O_5$  can reduce TCF to almost zero values for the given materials. Studies on the barium titanate materials revealed that changes in the Ba/Ti ratio result in the appearance of second phases, some of which can have TCFs opposite to that of the major compound [15]. Thus, deviation from stoichiometry changes the behavior of the whole system and can be used to manipulate the value of the temperature coefficient and microwave losses.

Zirconium titanate based ceramics have been recognized as temperature stable materials [15]. Newnham demonstrated that  $ZrTiO_4$  has orthorhombic structure [17] with c-axis dimensions highly sensitive to the processing conditions [18]. The critical annealing range (1130-1170 °C) indicates an onset of cation ordering. Azough [19] found a correlation between the ordering of the system and the quality factor: the quality factor of zirconium titanate based material increases with increasing degree of ordering.

Subsequent experiments showed that doping with Sn stabilizes the structure and shifts TCF to almost zero value. Christoffersen *et al* [20] reported  $\tau_f = 1 - 5 \text{ ppm}/K$  and  $Q = 7000 - 10000$  for  $Zr_{1-x}Sn_xTiO_4$  (where  $0 < x < 0.4$ ), making this compound suitable for applications in the microwave range.

Although titanate systems show relatively high quality factors, their low values of the dielectric constants do not allow the further miniaturization of the microwave components. One of the attempts to create materials with high  $\epsilon_r$  were studies on  $BaO \bullet R_2O_3 \bullet TiO_2$  ceramics [16] (where R stands for rare-earth elements, namely Nd,La,Sm,Pr). Kolar *et al* [21] demonstrated that 1:1:4 and 1:1:5 ratios in  $BaO \bullet R_2O_3 \bullet TiO_2$  materials produce the highest Q and  $\epsilon_r$  values ( $\approx 80$  and  $\approx 3000$ , respectively). While high dielectric constants can be utilized to reduce the size of the dielectric resonator, low values of the quality factor could not be tolerated with respect to the selectivity and optimum bandwidth for some applications.

Later, a series of ceramics  $Ba(Zn,Ta)O_3$ ,  $Ba(Co,Ta)O_3$ ,  $(1-X)Ba(Mg,Ta)O_3 - X Ba(Sn,Ta)O_3$  (with  $Q > 10,000$  and  $\epsilon_r$  ranges from 30 up to 50) based on perovskite type materials have been reported [10,22-24].

## 2.2 Perovskite Structure ( $ABO_3$ )

Generally, perovskite type materials can be described by the formula  $ABO_3$ , and structurally represent a cubic cell with a small ion, B at the center, larger A ions situated at the corners, and oxygen ions on the edges (fig.2.2). The size of the unit cell depends on the ionic radii of the A and B site cations and is usually around 4 $\text{\AA}$ . Depending on the values of the ionic radii of A and B ions, the unit cell tries to minimize its volume, which often results in structural changes and unit cell distortion.

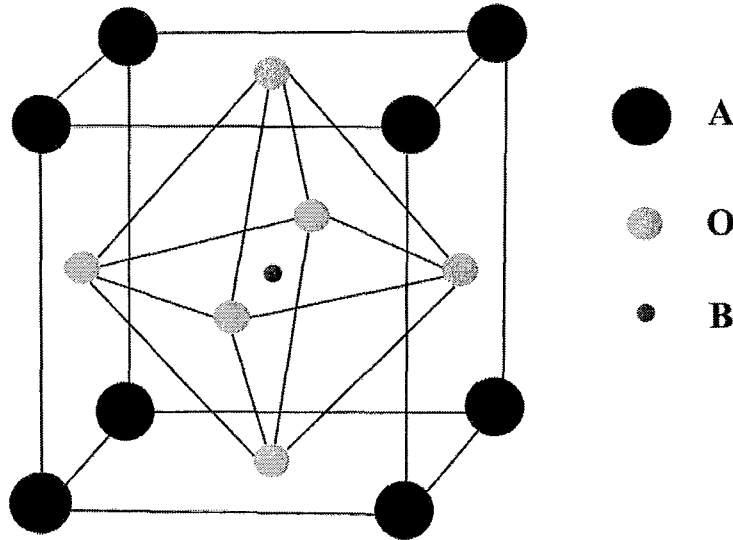


Fig.2.2 Perovskite type structure

The dielectric characteristics of perovskite materials have been investigated by far infrared reflection spectroscopy [2,25,26], phase transitions [27,28] and lattice vibrations [29,30]. Takeshi Takahashi [31] performed first-principles investigations of the phase stability of perovskite type structures. Most of the investigations, however, concentrated on the experimental determination of A and B site ions that would result in higher Q-factors and zero TCF.

Experimentally it was found that perovskites based on the formula  $Ba(B'_{1/3}B''_{2/3})O_3$ , where  $B' = \text{Zn}, \text{Mg}$  and  $B'' = \text{Ta}$  possess the lowest losses and have dielectric constants on the order of 30 [32].

Galasso in the 1960s showed that if more than one type of ion with large difference in size or charge is present on the B-site in a 1:2 mixture it is possible that they will be ordered along (111) crystallographic planes [33]. The long-range ordering accompanied with displacement of oxygen ions leads to a hexagonal structure with repeating sequence (... $B' - B'' - B'' - B'$ ...) along (111) planes [33,34]. Experimental investigations of the structure and the electronic properties of the tantalum based system showed that microwave losses (and hence quality factor) strongly depend on the degree of ordering of B-site cations. The long-range cation ordering can be induced by annealing at higher temperatures (above 1400 °C) and for a longer time. For instance, in  $Ba(Zn_{1/3}Ta_{2/3})O_3$  and  $Ba(Mg_{1/3}Ta_{2/3})O_3$ , ordering results in changes of the Q value from 500 to 35,000 at 10GHz [35,36].

A number of publications have been devoted to the study of B-site cation ordering in perovskite materials by taking advantage of X-ray diffraction techniques [37]. One of the examples of the research conducted in this direction is the study of Kawashima and Matsumoto [35,36] on the influence of cation ordering on the quality factor induced by changing annealing times and firing temperatures.

The principal differences in the X-ray spectra between disordered and ordered perovskite structures are the appearance and relative changes in the intensities of the superlattice peaks originating from the chemical order. It is common to evaluate the degree of ordering by a  $c/a$  ratio where ‘ $c$ ’ and ‘ $a$ ’ are lattice parameters of the unit cell. For a disordered structure  $c/a$  is close to unity (for the completely disordered

cubic phase with symmetry  $Pm\bar{3}m$ ,  $c/a=1$ ). Full ordering (trigonal  $P\bar{3}m1$  ordered cell) would give  $c/a>1.22$  [16].

Examples of the XRD spectra for cubic and hexagonal phases of some perovskites used in this work as well as conditions such as firing temperature used to induce ‘phase transition’ will be presented in the section devoted to the X-ray diffraction technique.

## 2.3 Dependence of Temperature Coefficient of the Dielectric Constant on the Structure of the Material

Almost all works on the application of perovskite type materials for microwave purposes have been conducted on an experimental basis: substances with different types of A and B ions (including two different atoms in the B-site sublattice) in different relative concentrations have been tested for lower losses and for the acceptable values of the temperature coefficient. So, for the experimentalists it would be desirable to have some guideline for the preparation of suitable dielectric materials. Work by Reaney *et al* demonstrated a correlation between the microwave properties of perovskites and parameters related to the structure of the material [38].

Reaney’s work is based on the results of Colla *et al* [39,40] that showed that the major factor influencing the behavior of  $\tau_\epsilon$  as a function of temperature and composition is the onset of tilt transition. In order to characterize changes in the symmetry of the structure, Megaw introduced the so called tolerance factor  $t$  [41]:

$$t = \frac{R_A + R_O}{\sqrt{2}(R_B + R_O)} \quad (2.2)$$

where  $R_A$ ,  $R_B$  and  $R_O$  are the ionic radii of the A-, B- and O-ions.

The perovskite phase will be created only for tolerance factors that are close to unity [38]. If the value of  $t$  is far from 1, perovskite composition will not be formed but rather a structure with some other form of symmetry will be created. An example of a material possessing a tolerance factor far from 1 is  $MgTiO_3$  ( $t=0.81$ ). In spite of the similarity of the given compound to the perovskite materials, magnesium titanate does not form in the perovskite structure but has ilmenite configuration [42].

Fig.2.3 shows the dependence of the temperature coefficient of the dielectric constant on the tolerance factor (and hence on the symmetry of the compound) for different barium and strontium based compositions. The list of acronyms used in fig. 2.3 is presented in Table 2.2.

At first, the value of the temperature coefficient of the dielectric constant smoothly decreases to its minimum ( $t=0.985$ ) and then abruptly rises again. According to [19] the value of the Q-factor depends on the symmetry of the system: structures with higher symmetry have larger quality factor. In fig.2.3, systems having higher symmetry have higher tolerance factor.

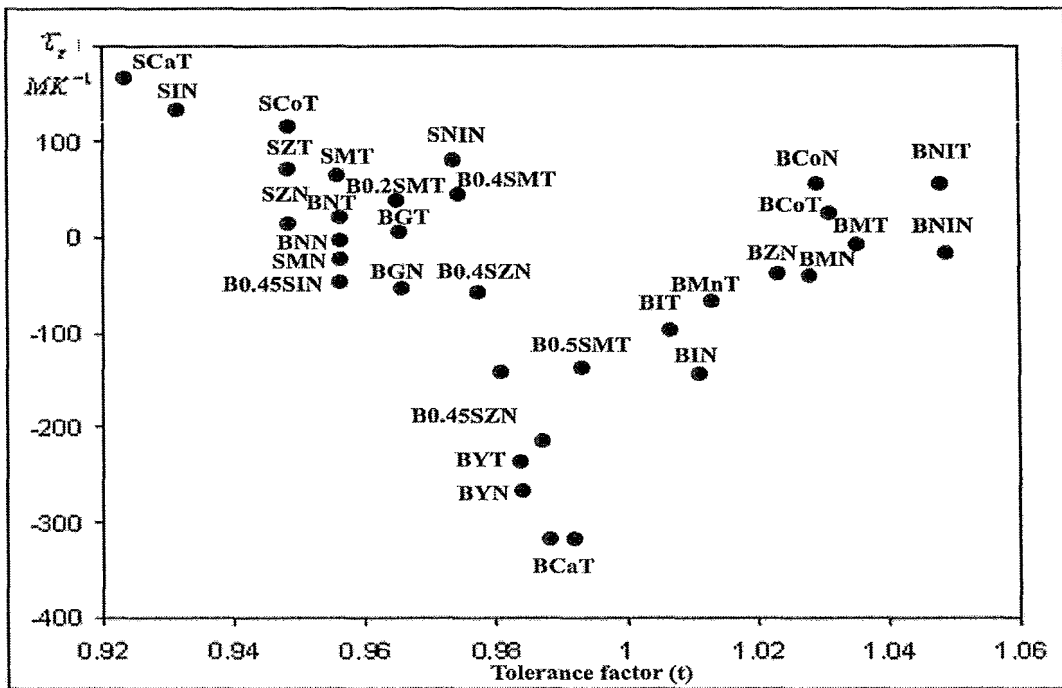


Fig.2.3 Dependence of the temperature coefficient of the dielectric constant on the tolerance factor for some Ba and Sr-based perovskites

Table 2.2 List of acronyms used in fig. 2.3

Abbreviation	Formula	Abbreviation	Formula
$B_x SZN$	$Ba_x Sr_{1-x} (Zn_{1/3}Nb_{2/3})O_3$	$SNiT$	$Sr(Ni_{1/3}Ta_{2/3})O_3$
$B_x SMT$	$Ba_x Sr_{1-x} (Mg_{1/3}Ta_{2/3})O_3$	$BNiT$	$Ba(Ni_{1/3}Ta_{2/3})O_3$
$B_x SIN$	$Ba_x Sr_{1-x} (In_{1/3}Nb_{2/3})O_3$	$BMnT$	$Ba(Mn_{1/3}Ta_{2/3})O_3$
$BNT$	$Ba(Nd_{1/2}Ta_{1/2})O_3$	$BMnN$	$Ba(Mn_{1/3}Nb_{2/3})O_3$
$BGT$	$Ba(Gd_{1/2}Ta_{1/2})O_3$	$BMgN$	$Ba(Mg_{1/3}Nb_{2/3})O_3$
$BYT$	$Ba(Y_{1/2}Ta_{1/2})O_3$	$SMgN$	$Sr(Mg_{1/3}Nb_{2/3})O_3$
$BCaT$	$Ba(Ca_{1/3}Ta_{2/3})O_3$	$BZT$	$Ba(Zn_{1/3}Ta_{2/3})O_3$
$SCaT$	$Sr(Ca_{1/3}Ta_{2/3})O_3$	$BNiN$	$Ba(Ni_{1/3}Nb_{2/3})O_3$
$BCoT$	$Ba(Co_{1/3}Ta_{2/3})O_3$	$SNiN$	$Sr(Ni_{1/3}Nb_{2/3})O_3$
$SCoT$	$Sr(Co_{1/3}Ta_{2/3})O_3$	$BCoN$	$Ba(Co_{1/3}Nb_{2/3})O_3$
$SZT$	$Sr(Zn_{1/3}Ta_{2/3})O_3$		

By combining the requirements for the system to give near zero TCF and acceptable values of the quality factor, one has to consider materials with  $t$  values ranging from 1.01 to 1.05.

So, before performing experimental research on the microwave properties of perovskite type materials one can estimate possible values of  $\tau_e$  and TCF just by using the ionic radii of the atoms [43] in the media.

## 2.4 Origin of the Dielectric Losses

Dielectric losses of the microwave resonators depend mostly on the losses in the dielectric medium itself (absorption of microwave energy in the waveguide system is negligibly small in comparison with that in the dielectric material) and are determined by the structure of the material [2].

By and large, dielectric losses can be classified as intrinsic and extrinsic. The first one arises in perfect (ideal) crystals because of the anharmonic lattice forces that mediate the interaction between phonons in the crystal. Any changes in the lattice structure will result in the material having different values of the quality factor. The tilting in the structure of perovskites that determines the value of the temperature coefficient of the dielectric permittivity also influences the value of the intrinsic dielectric losses.

Extrinsic losses are characteristic for inhomogeneous crystals and appear due to the scattering of the phonons on impurities, dislocations, grain boundaries and second phases.

The data on the dependence of microwave losses on the grain size is controversial. Some authors reported increases in the dielectric losses with increasing grain size [44], but for example, for titanium oxide [45] they did not observe any correlation between the grain size and losses in the material.

The presence of second phases which can be useful to tune TCF, usually degrades the value of the Q-factor of pure ceramics [46]. So, it is desirable to obtain single phase composition.

Point defects that often occur in the bulk material initiate one phonon scattering process that can significantly increase microwave losses. From this point of view it would be advantageous to obtain defect free material. In the particular case of the perovskite system, for which it was mentioned that the quality factor depends on the degree of ordering, certain amounts of point defects on the B-sublattice can significantly increase the ratio of cation ordering.

## 2.5 Niobium vs Tantalum Based Perovskites

Among the first perovskites that were successfully used in microwave applications were tantalum based ones [22-24]. The quality factors and the dielectric constants of  $Ba(B_{1/3}Ta_{2/3})O_3$  were around 16,000-40,000 and 20-30, respectively. In spite of good characteristics for applications in microwave resonators, the cost of raw

materials ( $Ta_2O_5$ ) and high sintering temperatures make production of tantalum ceramics economically unprofitable.

Niobium oxide  $Nb_2O_5$  is isostructural with  $Ta_2O_5$  and both niobium and tantalum ions have identical ionic radii (0.64Å). So, it seems logical to substitute niobium for tantalum in the process of preparation of microwave ceramics [25,47].

Several authors investigated dielectric resonators based on  $Ba(B'_{1/3}B''_{2/3})O_3$  perovskites (where  $B'=\text{Co,Mg,Zn,Ni}$  and  $B''=\text{Nb}$ ). For example, Reaney *et al* studied pure zinc and magnesium based perovskite structures [48]. Preliminary measurements resulted in quality factors ranging between 12,000 and 17,000 for barium magnesium perovskite (BMN) and barium zinc perovskite (BZN), respectively and temperature coefficients having positive values. In order to tune TCF to zero it was suggested to add small amounts of  $Ba(Ga_{1/2}Ta_{1/2})O_3$  (BGT). For BZN materials the highest quality factor was achieved for 5% of BGT ( $Q=34,900$ ), but to tune TCF to zero the concentration of BGT should be increased up to 10% (quality factor drops only to 32000).

For the  $Ba(Co_{1/3}Nb_{2/3})O_3$ (BCN) system, Cheol-Woo Ahn *et al* reported negative values of the temperature coefficient of resonance frequency ( $\tau_f \approx -10 \text{ ppm/K}$ ) and a quality factor on the order of 11,000 [49].

Relatively high values of the quality factor and positive and negative values of TCF for BMN, BZN and BCN, respectively, determined the choice of ceramic composition used in the present studies.

Analogously to the tantalum based system, ordering on the B-sublattice results in decreases of the microwave losses. But in contrast to the tantalum materials, for the

niobium based system it was observed that B-site ordering is a rather sluggish process [50] that requires prolonged sintering times.

For  $Ba(B'_{1/3}Ta_{2/3})O_3$  materials the most common way to observe ordering is through X-ray measurements. The scattering power of the samples depends on the  $B'/B''$  charge ratio. Unfortunately, for niobium based perovskites the charge ratio is close to unity, resulting in a decreased sensitivity of the X-ray diffraction technique.

## **2.6 X-ray Diffraction: Magnesium Niobate Perovskites as an Example of Disordered-Ordered Transition**

Janaswamy *et al* studied ordering in BMT and BMN perovskites sintered in the temperature range 1300-1600 °C by means of X-ray diffraction [51].

It was reported that after firing at 1300 °C both perovskites exist in the cubic phase (fig.2.4, ref. [51]). By increasing the sintering temperature to 1400 °C ordering was observed in both compounds. Subsequent refinement showed, however, that the degree of ordering was different: 7.9% of BMN versus 8.6% for BMT possess hexagonal structure. By raising the temperature the splitting in the amount of perovskite that exists in the ordered phase increases. At 1600 °C X-ray diffraction revealed complete ordering for BMT ceramics. At the same time, only 22.5% of BMN was found to be in the hexagonal phase.

Those observations just indicate that the degree of ordering depends on the charge imbalance between B-site cations and the difference in the ionic radii. For the

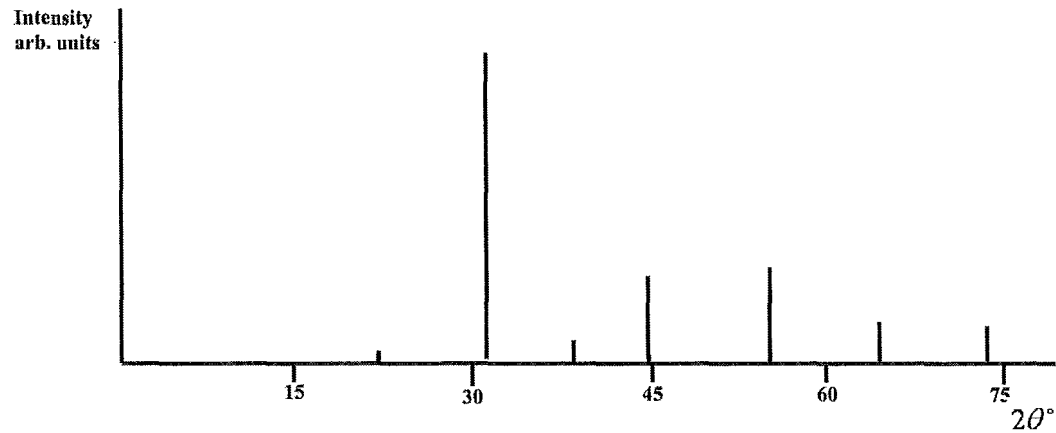


Fig.2.4 X-ray diffraction pattern for cubic phase of  $BaMg_{1/3}Nb_{2/3}O_3$  [51]

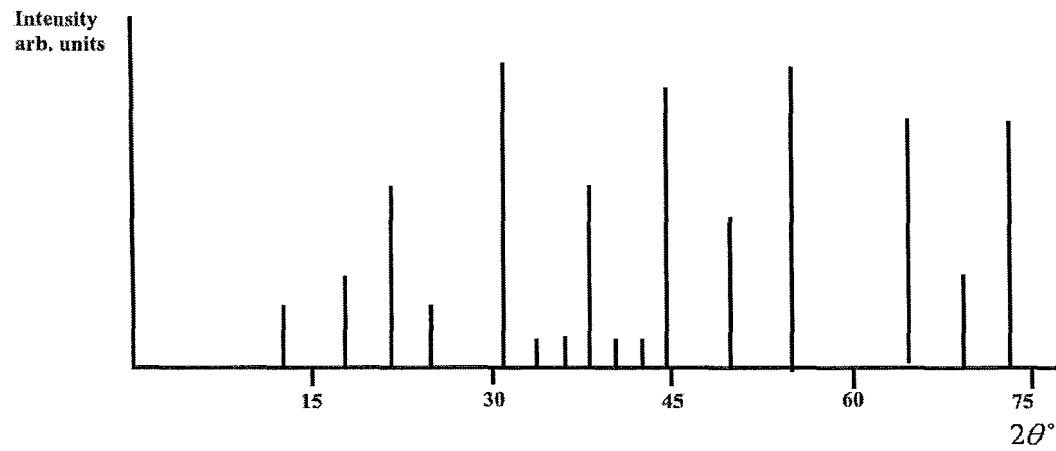


Fig.2.5 X-ray diffraction pattern for hexagonal phase of  $BaMg_{1/3}Nb_{2/3}O_3$  [52]

BMN system complete transformation to the hexagonal structure was achieved only after sintering at 1800 °C . Fig.2.5 (ref. [52]) provides an X-ray spectrum for the ordered phase of the BMN type perovskite. As was mentioned in the beginning of the first chapter (compare fig.2.4 and fig.2.5) the major differences in the X-ray spectra for the two phases are changes in the relative intensities of the main peaks (at 31°, 44°, and 55°) and appearance of the small peaks in the region  $2\theta = 30 - 45^\circ$ . The main peaks can be used to identify “disordered-ordered” transitions because of their high intensities since the appearance of peaks with small intensities often can be hidden in the background signal.

Several authors tried to take advantage of other measuring techniques to observe B-site cation ordering. For instance, Dmowski *et al* [53] utilized synchrotron X-rays and pulsed neutrons to observe changes along the (111) plane in the perovskite system. Unfortunately, those kinds of experimental setups are very costly and are not widely available for experimental groups. Studies of Moreira *et al* [54] employed Raman spectroscopy for this problem.

Here, we are trying to make use of positron annihilation spectroscopy accompanied by X-ray measurements to detect ordering and defect structures in  $Ba(B'_{1/3}Nb_{2/3})O_3$  perovskites. As will become clear from the next Chapters, positron annihilation spectroscopy is a technique that is very sensitive to the lattice parameters and defects in materials. By taking advantage of positron annihilation spectroscopy one would be able to simultaneously investigate the existence and concentration of defects and possible impurities as well as the structure of the lattice.

## **Chapter 3**

### **Positron Annihilation Spectroscopy**

#### **3.1 Basics of Positron Annihilation Spectroscopy**

The existence of an antiparticle of the electron was predicted almost eighty years ago by Dirac. Twenty years later (1942) first experiments involving electron-positron annihilation were conducted: Behringer and Montgomery studied the Fermi surface in metals and alloys [55].

The positron, being the antiparticle of the electron, has the same physical properties except for the opposite charge. Coulomb interaction between the positive charge of the positron and the negatively charged electronic cloud is utilized by positron annihilation spectroscopy (PAS) to study defects in materials [56-58].

PAS is based on the trapping of positrons by an attractive potential of the defects created by missing nuclei. Defects can be created by vacancies, vacancy agglomerates, dislocations or grain boundaries. The sensitivity of PAS is on the order of one defect per ten million atoms. Positron annihilation spectroscopy has been successfully applied to the study of negative or neutral defects but it is insensitive to positively charged ones.

Positron-electron interaction studies can be classified into two main groups, according to their sensitivity to changes in the distribution of density and momentum of electrons in the studied materials. The influence of the electron density distribution on the annihilation characteristics of positrons is used in positron annihilation lifetime spectroscopy. The second group consisting of Doppler broadening spectroscopy and angular correlation of annihilation radiation spectroscopy measures the changes in

either the energy or the collinearity of the emitted gamma radiation resulting from the interaction of positrons with the electron cloud having different momentum.

### 3.2 Source of Positrons

The most commonly used source for positron production is sodium-22. The advantages of this material are: a relatively long half life (2.6 years), so during an experiment the intensity of the source can be considered as constant; relatively large rate of positron production (about 90%); production of positrons is accompanied by the emission of a 1.27MeV gamma quantum that can be used to identify the birth of the positron; ease of source preparation process (radioactive source can be prepared by evaporation of  $^{22}Na$  from chloride or acetate salts) and small biological half life (sodium source is safe in case of accidental contamination of

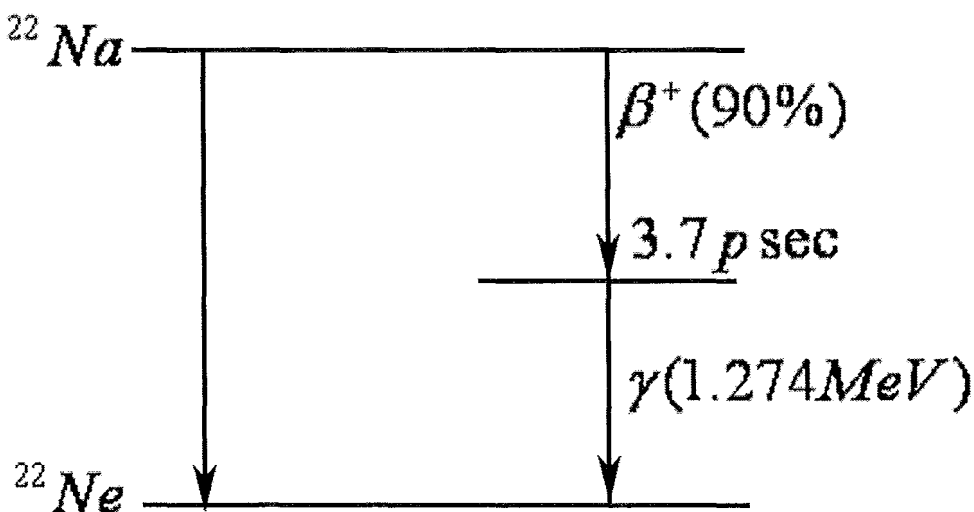


Fig. 3.1 The decay scheme of the radioactive isotope of sodium-22

the laboratory personnel). The decay scheme of  $^{22}Na$  is shown in fig.3.1 and can be described by equation (3.1):



where  $\nu_e$  and  $\gamma$  means neutrino and gamma ray, respectively, and  $\beta^+$  stands for positron.

Roughly 90% of decays of  $^{22}Na$  occur to the excited state of  $^{22}Ne$  with the release of a positron and an electron neutrino. The transition from the excited state of  $^{22}Ne$  to its ground states takes place after 3.7 psec and is accompanied by the emission of a 1.27 MeV gamma quantum. This fact plays an important role in positron lifetime spectroscopy since the time difference between the emission of the positron and of the gamma ray is small in comparison with the positron lifetime in matter so the  $\gamma$ -ray can be used to identify the birth of the positron. The transition dipole moment (regulating the probability of the nuclide making the transition from one energy state to the other) between the ground state of sodium-22 and the ground state of neon is small, so less than 1% of the decays happen without 1.27 MeV gamma ray production.

### 3.3 Positron-Matter Interaction

A positron approaching a material's surface can be scattered back or penetrate into the material. Initially, the kinetic energy of positrons is much larger than the thermal energy of diffusion [56]. The difference between these two energies is transferred to the crystal in the form of core ionization processes (for high energy positrons) and phonon scattering (for positrons with energies of several electronvolts).

The process of transferring energy to the material is called thermalization. The energy transfer rate is not uniform and depends on the initial energy of the positron: the energy-loss rate is larger for  $\beta^+$  with higher energies. As a matter of fact, high-energy positrons spend most of the time with energies just above equilibrium. That is why high and low energy positrons thermalize almost simultaneously [59]. The process of thermalization occurs within several picoseconds (for experiments conducted at room temperature, but much longer for low-temperature measurements (see, for example, ref.[60])) after positron implantation in the sample. So, in most of the experiments the time the positrons exist before thermalization can be neglected.

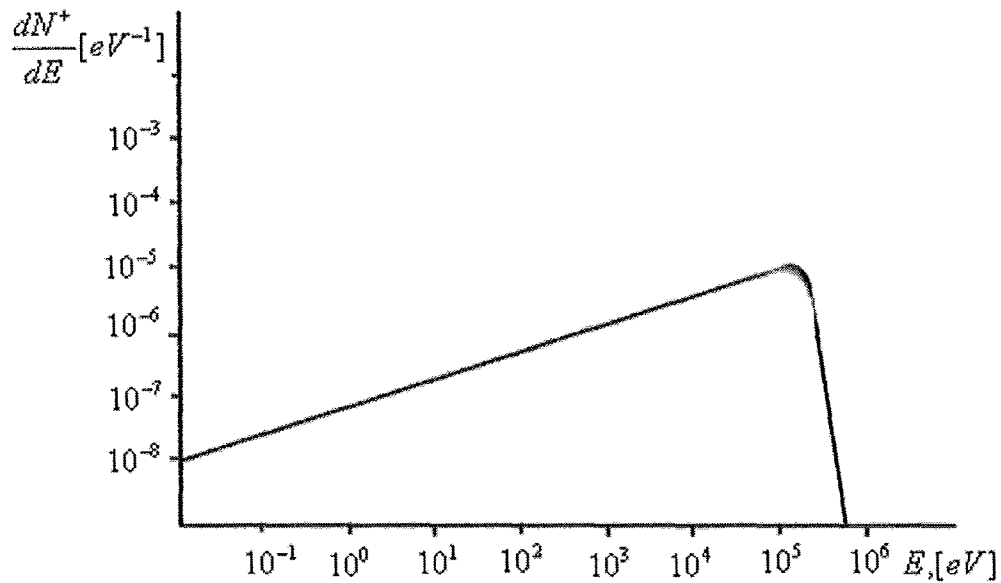


Fig.3.2 Emission spectrum of sodium-22

The penetration depth of positrons depends on the initial energy of the  $\beta^+$  particle. The energy spectrum of positrons emitted from sodium is broad and ranges from several electronvolts up to several kiloelectronvolts (fig.3.2). Thus, the

distribution of positrons within the sample depth is not uniform and can be described by the following empirical equation [61]:

$$P(x) = \alpha \cdot e^{-\alpha \cdot z} \quad (3.2)$$

where  $\alpha$  is the absorption coefficient that depends on the density ( $\rho[g/cm^3]$ ) and atomic number ( $Z$ ) of the material. It was found experimentally [62] that

$$\alpha = \frac{2.8\rho Z^{0.15}}{\bar{E}^{1.19}} \quad (3.3)$$

where  $\bar{E}$  is the mean positron energy (for  $^{22}Na$  it equals 0.15MeV). For most of the samples, the mean penetration depth is less than several hundreds of microns. This defines the lower limit for the thickness of the sample in order to ensure that all annihilations happen inside of the studied specimens.

Equation (3.2) describes the positron implantation profile right before their diffusion in the sample.

### 3.4 Diffusion of Positrons

After thermalization positrons diffuse in the samples and behave as charged particles. The process of diffusion can be described as the evolution of the positron wave function in momentum and real space [57].

In a defect free structure where the atomic position is periodic, the shape of the positron wave function is also periodic. Because of the positive potential of the nuclei the probability for positrons to be found at the center of the atom is the smallest peaking in the interstitial regions where the influence of the positive charge of the

nuclei is minimal. In case of changes in the periodicity of the structure that can be caused either by impurities or missing atoms, positrons become localized or trapped. Energy eigenvalues of the positrons trapped into defects are lower than those for the delocalized positron. As a result, the difference in the energy is transferred to the host material or matrix.

In most practical cases the density of the electron cloud in defects is different from that in the matrix. Particularly, vacancy type defects exhibit reduced electron density. So, positrons trapped in the vacancy have longer lifetimes (called defect lifetime,  $\tau_d$ ) in comparison with the lifetime of positrons annihilating from the delocalized state (bulk lifetime,  $\tau_b$ ).

The tail of the positron wave function extends over many lattice periods pointing to the possibility of the positrons traveling several hundreds of nanometers before they annihilate. While diffusing along the structure, positrons probe changes in the electron density and lattice periodicity. So, finally, when positrons annihilate by emitting two gamma rays, these contain information about the electronic cloud along the way the positrons diffused in the sample. Because of the conservation of mass of the “electron-positron” system the energy of the emitted gamma rays is equal to 511keV, each, and application of momentum conservation results in those quanta traveling in opposite directions.

In spite of the simplicity of the processes that occur after positrons penetrate materials, it is quite difficult to extract materials parameters. Different techniques are used to obtain information about the electron distribution within the studied specimen. The present work takes advantage of lifetime and Doppler broadening spectroscopy

accompanied by theoretical calculations to study defects in columbite and perovskite type materials.

### **3.5 Trapping Model and Its Connection to the Experiment**

A description of positron trapping in matter was first given by Bertolaccini and Dupasquier as early as 1970 [63]. They first formulated the so called trapping model giving a qualitative description of the positron behavior in the material after thermalization.

The validity of the trapping model is determined by the following conditions [56]:

First, defects in the material should be distributed homogeneously within the volume and do not interact with each other. Second, the positron trapping in the defects before thermalization should be negligibly small.

As it will be clear from the experimental part, only one defect type will be observed in the studied samples. So, in the following we will concentrate on the description of the so-called one defect trapping model. More general cases of positron trapping in two or more types of defects can be found, for example, in [56].

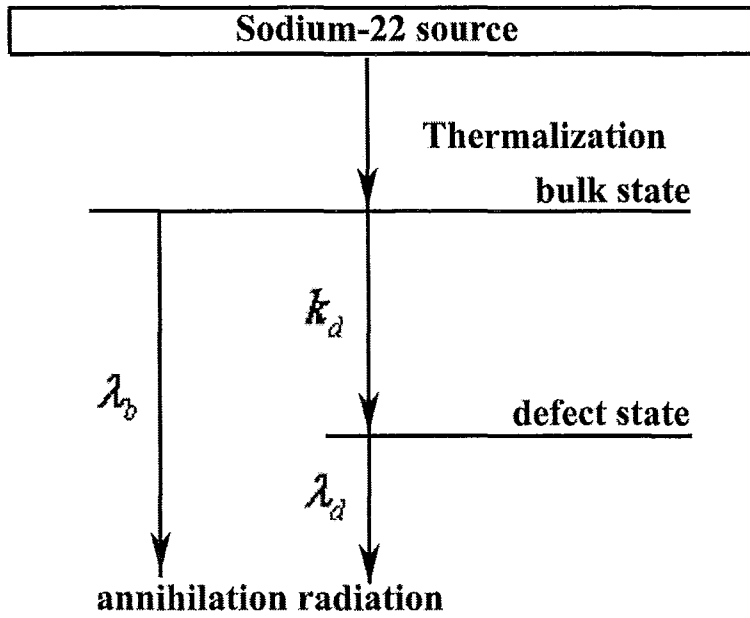


Fig.3.3 Scheme of the trapping model with one defect type

According to the trapping model, after thermalization at  $t=0$  the positron can exist in only one state which is bulk state (the so-called delocalized or Bloch state, fig.3.3). From this state the positron can either annihilate with the annihilation rate  $\lambda_b$  or be trapped. The transition between the bulk and defect states is described by the trapping coefficient  $k_d$ . From the defect state the annihilation rate is described by  $\lambda_d$ . This model does not consider thermally induced detrapping that can exist in the real materials.

If one considers the occupational probability of the bulk state in the initial moment to be equal to unity, then the annihilation of positrons from the Bloch state and their transition to the localized state can be described by the rate equation:

$$\frac{dn_b}{dt} = -(\lambda_b + k_d)n_b(t) \quad (3.4)$$

Positron trapping in the defect state with their further annihilation is described by the balance rate equation:

$$\frac{dn_d}{dt} = -\lambda_d n_d + k_d n_b(t) \quad (3.5)$$

According to the initial assumptions that there is no trapping of the positron before thermalization the initial conditions for t=0 can be formulated as:

$$n_b(0) = N_0 \quad (3.6)$$

where  $N_0$  is the total number of positrons implanted into the sample and

$$n_d(0) = 0 \quad (3.7)$$

In this case the solution of the differential equations (3.4) and (3.5) represents the decay spectrum of the positrons:

$$D(t) = I_1 \exp(-\frac{t}{\tau_1}) + I_2 \exp(-\frac{t}{\tau_2}) \quad (3.8)$$

where  $\tau_{1,2}$  and  $I_{1,2}$  denote lifetimes and their relative intensities extracted from the experimental spectrum. Their connection to the values operated within the trapping model is established by the following equations:

$$\begin{aligned} \tau_1 &= \frac{1}{\lambda_b + k_d} & \tau_2 &= \frac{1}{\lambda_d} \\ I_1 &= 1 - I_2 & I_2 &= \frac{k_d}{\lambda_b - \lambda_d + k_d} \end{aligned} \quad (3.9)$$

In practice, an experimental spectrum is measured as a number of annihilating positrons per time channel, and therefore, represents an absolute value of the time derivative in (3.8):

$$N(t) = \left| \frac{dD(t)}{dt} \right| = \frac{I_1}{\tau_1} \exp(-\frac{t}{\tau_1}) + \frac{I_2}{\tau_2} \exp(-\frac{t}{\tau_2}) \quad (3.10)$$

The values of  $I_1, I_2, \tau_1$  and  $\tau_2$  and, hence, bulk and defect lifetimes, can be obtained by fitting (3.10) to the experimental data.

While  $\tau_b$  and  $\tau_d$  give some information about the structure of the sample and defects sizes, the real physical value that can be used further for the sample preparation is the defect concentration  $C$ . It is evident that the higher the concentration of the defects in the sample the higher the positron trapping rate. So, the positron trapping rate is proportional to the defect concentration:

$$C = \frac{1}{\mu} k_d \quad (3.11)$$

where  $\mu$  is a constant for a given material and the defect trapping rate is defined through the positron lifetime output parameters as:

$$k_d = \frac{I_2}{I_1} \left( \frac{1}{\tau_b} - \frac{1}{\tau_d} \right) = I_2 \left( \frac{1}{\tau_1} - \frac{1}{\tau_2} \right) \quad (3.12)$$

In order to calculate the defects' concentrations, the coefficient  $\mu$  has to be independently found from other kinds of experiments without involving positron results.

## 3.6 Theoretical Background

Positrons are very sensitive to the electron density distribution. The ability of positron to be localized in the defects' sites can be used to study defects in the material. The atomic structure of the material determines the electron density distribution inside of the studied material. This results in a dependence of the positron data on the material structure.

However, to fully understand experimental results an accompanying model that is able to describe the positron-electron interaction in the medium is needed.

The following section deals with the description of the theoretical model used to explain experimental results obtained by positron lifetime spectroscopy.

### 3.6.1 Local Density Approximation (LDA)

The positron lifetime is the inverse of the annihilation rate, which is proportional to the overlap of the electron and positron densities:

$$\lambda = \frac{1}{\tau} = \pi r_e^2 c \int dr n_-(r) n_+(r) g(n_-(r), n_+(r)) \quad (3.13)$$

where  $r_e$  and  $c$  are the classical electron radius and the speed of light, respectively.

$g(n_-(r), n_+(r))$  is called an enhancement factor and takes into account the increase in the annihilation due to the screening cloud of the electrons around the positron. From (3.13) it follows that calculation of  $\tau$  represents three tasks. First, the electron density should be calculated self consistently. Then, the positron charge density is found. Finally, the integral in (3.13) is evaluated [64].

For the defect free (perfect) lattice the positron density is negligibly small (delocalized positrons) and does not influence the electronic structure of the system. In this case the calculation of the positron states in the solid can be based on the Density Functional Theory (DFT) [65]. In more general cases of positron trapping in solids the positron density can be on the order of that of the electrons and the influence of the positive charge on the distribution of electrons can not be neglected. In order to describe the “positron-electron” system usually a two component density functional theory (TCDFT) is applied [66].

In TCDFT the total energy of the positron-electron pair is written as a functional of electron and positron densities. In the conventional scheme the electron density is first calculated without the effect of positrons. The Schrödinger equation for electron states can be written in the form:

$$[-\frac{1}{2}\nabla^2 + V_{ion}(r) + V_{Hartree}(r)]\psi^- = E^-\psi^- \quad (3.14)$$

where the  $V_{ion}(r)$  term is responsible for the Coulomb interaction with ions and  $V_{Hartree}(r)$  arises due to the interaction with the electron charge density. By solving equation (3.14) one can find the electron wave functions for the different states. In the Kohn-Sham method [67] the electron density is obtained by summation of the wavefunctions over all occupied states:

$$n_-(r) = \sum_{E_i < E_F} |\psi_i^-(r)|^2 \quad (3.15)$$

where  $E_F$  is the Fermi energy. In the material, the effective potential felt by positrons consists of the Coulomb part and the electron-positron correlation part. So, for positrons the Schrödinger equation can be written as [64]:

$$[-\frac{1}{2}\nabla^2 - V_{ion}(r) - V_{Hartree}(r) + V_{corr}(r)]\psi^+ = E^+\psi^+, \quad (3.16)$$

from which the density of positron is calculated as

$$n_+(r) = \sum_i^{N_+} |\psi_i^+(r)|^2 \quad (3.17)$$

where  $N_+$  is the number of the positrons in the system.

For the calculation of electronic states in solids the local density approximation (LDA) has been highly successful and was taken as a starting point for the evaluation of the “electron-positron” correlation potential. In LDA, the correlation potential is defined as one that the positron would feel in a free homogeneous electron gas. By treating core and valence electrons in the same way LDA usually overestimates the role of the valence electrons in the process of annihilation. Numerous calculations based on LDA for bulk transition metals involving d-electrons gave high annihilation rates in comparison with experiments [67,68]. Only for systems with slowly varying electron densities LDA produced results close to the experimental values [68]. By employing the local density approximation one obtains lifetimes that are too short in comparison with the experimental data.

Thus, the main drawbacks of LDA are:

- a) too diffuse electron densities in atoms that result in overbinding in molecules and solids
- b) underbinding of electrons in atoms.

To decrease the influence of core electrons on the positron annihilation rate Kaiser and Sterne suggested using  $g(n_-(r), n_+(r)) = 1$  for core electrons [69]. In the literature, this approach was called the independent particle model (IPM) and gave

results far from the experimental ones. The next step in the treatment of the “electron-positron” interaction was the formulation of the so-called Generalized Gradient Approximation where the electron density is considered as a gradient function [70].

### 3.6.2 Generalized Gradient Approximation (GGA)

In GGA the effect of nonuniform electron density is managed by the ratio of density variation on the local length scale ( $n/|\nabla n|$ ) and the local Thomas-Fermi screening length ( $1/q_{TF}$ ) [68,71,72]:

$$\varepsilon = \frac{|\nabla n|^2}{(nq_{TF})^2} \quad (3.18)$$

This parameter describes the change of the electron density in the vicinity of the positrons. For a uniform electron gas that corresponds to the local density approximation,  $\varepsilon = 0$ . In case of rapid density variations  $\varepsilon$  is equal to  $\infty$ . Homogeneous and fast changing density distributions are two limiting cases. In order to interpolate between them the density variation can be represented in the form

$$\Delta n_{GGA} = \Delta n_{LDA} e^{-\alpha\varepsilon} \quad (3.19)$$

From here, the enhancement factor can be written as

$$g_{GGA} = 1 + (g_{LDA} - 1)e^{-\alpha\varepsilon} \quad (3.20)$$

where  $\alpha$  is a parameter that can be obtained by fitting theoretically calculated results to the experimental data. Values of  $\alpha$  vary between 0 and 1. The widely used value of  $\alpha$  that gives the best fit is  $\alpha = 0.22$  [68].

By putting  $\alpha = 0$  into (3.20) one obtains  $g_{GGA} = g_{LDA}$  corresponding to the local density approximation.

In general, GGA gives results closer to the experimental data (rather than LDA) for finite systems and metallic surfaces [73,74]. The reason is that interaction in such kinds of systems is described by the tail of the wavefunction for which GGA gives a better approximation.

### 3.6.3 Enhancement Factor

The final part of the lifetime calculation is to derive an enhancement factor that would properly describe the electron-positron interaction.

Fig.3.4 shows the dependence of the calculated lifetime on the density parameter. The dotted line shows results of a scaled proton approximation [77] which gives a lower bound for the positron lifetime. All lines converge to the value of 500psec that is the average lifetime of positronium in the material.

Several attempts to approximate the dependence of the lifetime on the density parameter have been made. Boronski and Nieminen used results of many-body calculations by Lantto [75] (shown in fig.3.4 as open circles) to derive the enhancement factor in the following form:

$$g_{LDA-BN} = 1 + 1.23r_s + 0.8295r_s^{3/2} - 1.26r_s^2 + 0.3286r_s^{5/2} + \frac{1}{6}r_s^3 \quad (3.21)$$

where  $r_s$  is the so-called density parameter.  $r_s$  is related to the density of the electron cloud by

$$r_s = \left( \frac{3}{4\pi n_e} \right)^{1/3} \quad (3.22)$$

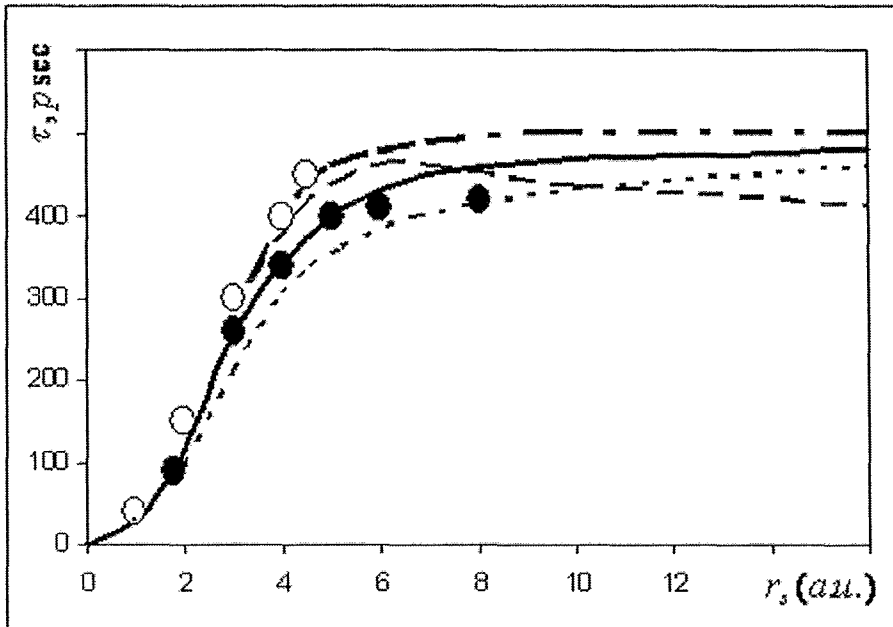


Fig.3.4 Lifetime versus density parameter. Filled and open circles denote results of many-body calculations of Arponen and Pajanne (ref.[76]) and those by Lantto (ref.[75]), respectively. The results obtained by scaled proton approximation are plotted as a dotted line (ref.[77]). The dash-dotted line shows Stachowiak-Lach results (ref.[78]). Dashed and solid lines are interpolation functions obtained by Boronski and Nieminen (ref.[65]) and Barbiellini (ref.[67]), respectively.

Barbiellini *et al* [68] derived the enhancement factor based on the results obtained by Arponen and Pajanne [76] (filled circles in fig.3.4 ):

$$g_{LDA-API} = 1 + 1.23r_s - 0.0742r_s^2 + \frac{1}{6}r_s^3 \quad (3.23)$$

The first two terms in (3.21) and (3.23) are responsible for the high density region that describes “electron-positron” interactions in transition metals, for which the bulk lifetime falls into a region around 100psec. The last term in both equations deals with the positronium limit, i.e., the low-density region.

As can be seen from fig.3.4 the Boronski-Nieminen enhancement factor fails to properly describe the lifetime behavior for the middle and low density part.

The Arponen-Pajanne enhancement factor in combination with the generalized gradient approximation with  $\alpha = 0.22$  gives lifetime values close to the experimental ones [67,68].

### 3.7 Doppler Broadening Technique

Positron lifetime spectroscopy is sensitive to the variation in the electron density in materials. It can be used to detect the concentration of impurities, missing atoms and other defects. In order to identify the “chemical nature” of defects in the lattice structure, however, other techniques should be used. In the present work, we use Doppler broadening spectroscopy to look for the possible presence of defects in the studied materials.

Doppler broadening spectroscopy is based on the conservation of momentum during annihilation of a positron-electron pair and utilizes the fact that different chemical elements have specific momentum distributions of core and valence electrons. Upon annihilation valence electrons mainly contribute to the low momentum part of the spectrum and core electrons give rise to the high-momentum region of the annihilation line [79].

Positrons trapped in vacancies annihilate primarily with the valence electrons. This results in different shapes of the low momentum part for materials with different defect concentrations: the larger the defect size or the higher its concentrations the narrower the annihilation line. So, the annihilation line from a sample containing defects is more intense and narrower in comparison with the defect free sample (see fig.3.5).

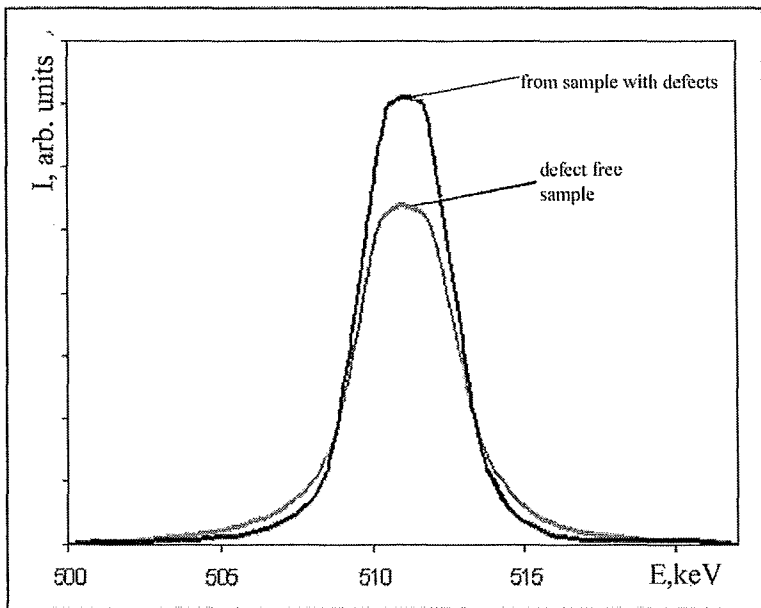


Fig. 3.5 Comparison of Doppler broadened annihilation line for defect free sample and sample containing defects

Core electrons are tightly bound to the nuclei and thus give rise to the high momentum part of the Doppler broadened line, which therefore contains information on the types of atoms in the vicinity of the annihilation site.

The 511keV annihilation line is Doppler broadened because of the longitudinal momentum component  $p_z$  of the annihilating electron-positron pair:

$$E_\gamma = (511 \pm \Delta E) \text{keV} \quad (3.24)$$

The vast majority of annihilation events take place after positron thermalization. Hence, the momentum of the positron is negligibly small and will be neglected. This results in an independence of the Doppler shift on the intensity of the source.

The direction of emission of upshifted and downshifted gamma rays is random. So, a detector placed at some distance from the positron source and sample can detect both annihilating gamma quanta [80]. The major drawback of a one

detector system is the high background signal which results from the Compton scattering, incomplete charge collection, pulse pile-up, environmental radiation and 1.27MeV quanta. The ratio of peak - to - background in a one detector experiment is quite low ( $\sim 10^3$ ) [81]. In a typical Doppler broadening experiment the energy shift,  $\Delta E$ , is several keV (usually information about chemical environment can be extracted from the part of the spectrum within a range of 5-9keV from the 511keV line). Because of the high potential barrier experienced by the positron near nuclei, annihilation with core electrons is less probable than that with the valence electrons. This results in the high momentum part having low relative intensity. Often, detection of the signal in the “wings” of the annihilation line is obscured by the background signal. In order to increase the signal-to-noise ratio a coincidence Doppler broadening setup was suggested by Lynn and Goland as early as 1976 [82]. It takes advantage of two detectors and is based on the fact that during the annihilation two 511keV quanta are emitted simultaneously in approximately opposite directions. By using a two detector system the signal-to-noise ratio can be improved by up to  $10^5$ .

A coincidence Doppler broadening setup with two high purity germanium detectors was used in the present research. The schematic of the experimental setup and all parameters relevant to these studies will be presented later in the experimental chapter.

### **3.8 Brief Introduction to the Results of Positron Lifetime**

#### **Spectroscopy for Perovskite Materials**

Up to now there are a limited number of publications on defect studies in perovskite type materials by employing positron annihilation spectroscopy.

In 2000, Ghosh and Nielsen theoretically predicted bulk and defect lifetimes as well as Doppler broadening curves for several perovskite structures ( $LaCoO_3$ ,  $BaTiO_3$  and  $PbTiO_3$ ) [83]. Their calculations became a reference-point for the other researchers in their attempts to explain experimental results.

$BaTiO_3$  (BTO) and  $PbTiO_3$  (PTO) are both ferroelectric perovskites. BTO can exist in cubic, tetragonal, orthorhombic and rhombohedral phases whereas PTO can adopt only cubic and tetragonal phases. It was reported that without doping  $LaCoO_3$  (LCO) possesses a cubic unit cell. In their calculations Ghosh *et al* used a cubic cell for the materials under consideration to construct a supercell (around 300 atoms) [84,85]. The results of their simulations are presented in Table 3.1.

Table 3.1 Results of bulk and defect lifetime calculations in some  $ABO_3$  perovskite type materials

	$LaCoO_3$	$PbTiO_3$	$BaTiO_3$
$\tau_b$ , psec	129	147	152
$\tau_A$ , psec	275	280	293
$\tau_B$ , psec	173	175	204
$\tau_o$ , psec	145	152	162

The bulk lifetimes for  $LaCoO_3$ ,  $PbTiO_3$  and  $BaTiO_3$  are predicted to be 129psec, 147psec and 152psec, respectively, indicating changes in the electron densities in these materials. For the vacancies on the A- and B-cation sites the values of the positron lifetimes are different, demonstrating the difference in charges of A and B ions. For the A-site ion the mean defect lifetime is on the order of 280psec. At the same time, for the B-ions Ghosh's calculations give lifetimes that are much shorter; around 180psec.

It is worth noticing that oxygen vacancies usually possess positive charge and, thus, positrons are insensitive to such kind of defects. Calculations of Ghosh and Nielsen give oxygen vacancy lifetimes that are different from the bulk values. The largest difference was observed for the LCO structure. This indicates that oxygen defects can change charge states from positive to neutral or negative and positron measurements can be used to reveal this kind of defect.

Lifetime measurements of  $La_{1-x}Sr_xCoO_3$  [86] showed the presence of two components: 138psec and 223psec. By taking advantage of the experimental results on the LCO system, Ghosh tried to correlate the accuracy of the method used in her calculations. The first value is very close to the bulk lifetime of LCO perovskite and the second, longer, value is attributed to the presence of the single vacancy. By changing the fractional part of Sr in  $La_{1-x}Sr_xCoO_3$ , a third component with  $\tau = 149\text{ psec}$  was separated and attributed to positron trapping in the oxygen defects indicating the validity of above mentioned hypothesis of a possible change in the oxygen charge state.

A series of experiments was performed on  $BaTiO_3$  perovskites [87]. After analysis of the experimental spectra, two components were obtained. The first (shorter) one (160psec) was associated with the bulk value of the BTO material, and the longer lifetime (318-347psec, depending on the conditions of the experiments) was connected to the formation of Ba vacancies. While the bulk value is in good agreement with the theoretical one, the slightly bigger difference between the experimental and theoretical values in the defect state was explained by possible formation of defect clusters around the Ba vacancy rather than a single Ba defect.

Gottschalk *et al* performed positron measurements on pressed powders of  $Pb(Zr_{0.6}Ti_{0.4})O_3$  [88]. For the lifetime calculations the one defect trapping model was applied giving a bulk value of 193psec. Relying on the calculations conducted by Ghosh on similar systems (around 150psec for the bulk value), Gottschalk assumed that such big differences can arise from the presence of more than one type of defects.

Today, ceramics are produced by pressed powder methods. In this case samples represent pieces of crystals separated by grain boundaries. Structurally, grain boundaries represent defects. One of the first attempts to introduce into consideration positron annihilation inside of the grain boundaries for perovskite type materials was made by Keeble *et al* who investigated defects in  $SrTiO_3$  (STO) [89]. Studying single crystal as well as ceramic STO, Keeble noticed that the long lifetime of 270-310psec can be ascribed both to the annihilation in A-site cation vacancies and grain boundaries.

### 3.9 Positron Annihilation at Grain Boundaries

Most attention of research groups in the field of positron annihilation spectroscopy has been concentrated on the theoretical and experimental studies of positron annihilation in the bulk and defects (or defect clusters) inside of matter. However, grain boundaries as well as dislocations in materials also represent traps for positrons and can significantly influence positrons' characteristics. Up to now there are just random publications regarding the application of positron annihilation between grains. The first attempt of a theoretical study of positron annihilation in grain boundaries belongs to Hubner *et al* [90].

After thermalization positrons start to diffuse in the material until they annihilate or are trapped in defects. In the case of grained material positrons can diffuse to the grain boundaries and be trapped on the grain surface. It is evident that the smaller the grain size the larger the fraction of positrons that can reach the grain surface, which will influence the annihilation spectrum. For materials with large grain size (in comparison with the diffusion length of the positron) the fraction of positrons trapped at grain boundaries is negligibly small and will be neglected during the analysis of positron results.

Hubner considered diffusion of positrons in homogeneously distributed spherical and ellipsoidal particles of the same size. In this situation the diffusion equation can be solved exactly without application of approximate methods.

Spherical and ellipsoidal particles cover almost all classes of particles that can be found in real materials. The former can approximate ball-like particles, and the latter resembles materials with rod-like or plate-like grains.

Practically important results of Hubner's simulations are presented in fig.3.6, which shows the fraction of positrons reaching the grain surface.

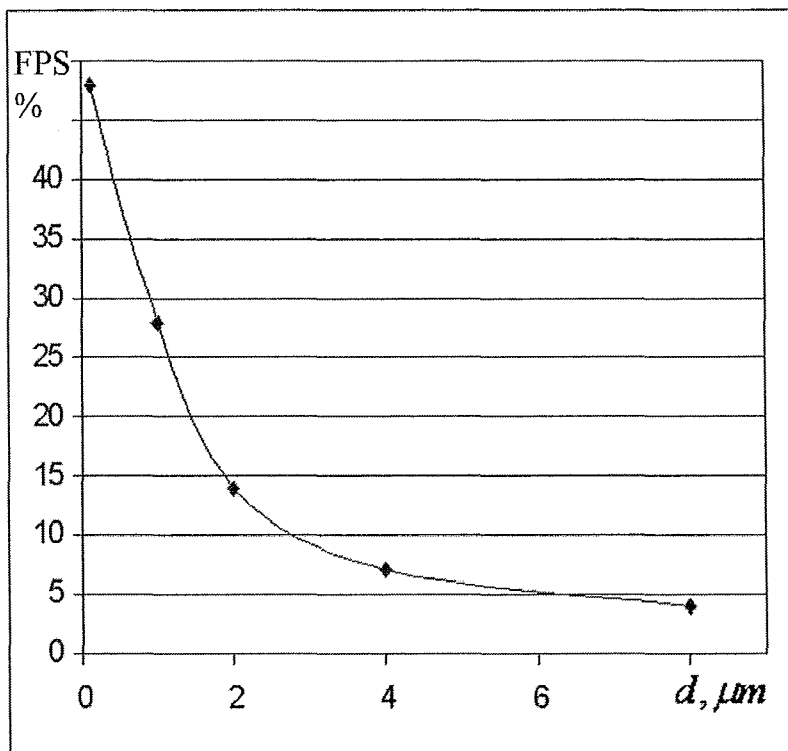


Fig.3.6 Results of Monte-Carlo simulations for fraction of positrons (FPS) reaching grain boundaries versus diameter of the grains

For materials with powder particles having diameters of ten microns or more, the fraction of positrons trapped in the grain boundaries is small and on the order of several percent. With decreasing particle size the number of positron trapped in the boundaries exponentially increases reaching up to 30% for particles with diameter around  $1\mu m$ . So, analysis of the experimental results obtained on materials with relatively small grain sizes should consider positrons annihilating on the grain surfaces. Also, a relatively high fraction of positrons reaching the boundaries of the

particles results in one important conclusion: if one wants to study defects in the contact region of the grains constituting the given material it is necessary to use media consisting of small particles.

Thus, results of simulations conducted by Hubner *et al* give a quantitative description of the part of positrons that are able to reach grain boundaries and can be used to explain the experimental data.

## Chapter 4

### Description of the Samples

The work described in this thesis was performed in collaboration with the V.I.Vernadskii Institute of General & Inorganic Chemistry, NASU (Kyiv, Ukraine). All samples used in positron measurements were obtained from Ukrainian colleagues and can be divided into two main groups according to the steps of the ceramics' formation during the preparation process: columbite and perovskite type materials.

This section briefly outlines the results of microwave measurements performed by the Ukrainian group (ref.[91], measurements of the quality factor as well as dielectric constant were performed at 10GHZ) and describes the choice of the samples' composition. Some of the results of Ukrainian colleagues will be used to facilitate an explanation of the results of positron annihilation spectroscopy.

Perovskite type materials were sintered in a two-step process: at first, columbite structures were obtained by mixing corresponding metal oxides with niobium pentoxide. Subsequent addition of the barium carbonate produces perovskite materials.

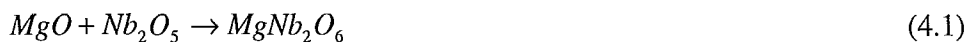
Preliminary measurements indicated that the composition of the perovskite structure greatly depends on the presence of second phases during columbite sintering. Second phases in  $B'Nb_2O_6$  used as a precursor for perovskite type materials result in the appearance of different barium niobates in the perovskite materials. Also, microwave measurements showed that the quality factor of the final product greatly depends on  $B'/Nb$  ratio, where  $B' = \text{Mg}, \text{Co}, \text{Zn}$  during the process of  $B'Nb_2O_6$

sintering. That is why the first part of the research was focussed on the investigation of the influence of structural defects on the microwave properties of stoichiometric and non-stoichiometric columbite samples.

## 4.1 Columbite Samples

### 4.1.1 Magnesium Columbite

Magnesium columbites were obtained by mixing powders of magnesium oxide with niobium pentoxide and subsequent firing at different temperatures. The formation of  $MgNb_2O_6$  started at 700 °C. By increasing the sintering temperature the concentration of  $MgO$  decreased. Full consumption of magnesium oxide was observed at 1200 °C. At this temperature just small traces of  $Nb_2O_5$  were found. Generally, the reaction describing the process of magnesium columbite formation can be written as:



As for the perovskite structure, it can be assumed that the electrophysical properties of the columbite type material depend on the distortion (ordering) of the unit cell. Changes in the symmetry of the structure can be achieved by varying the Mg/Nb ratio.

The first set of  $Mg_{1-x}Nb_2O_6$  samples (where  $x=-0.03, -0.01, 0, 0.01, 0.03$ ) were sintered in the presence of air at 1400 °C for 4 hours. The results of microwave measurements are presented in fig.4.1.

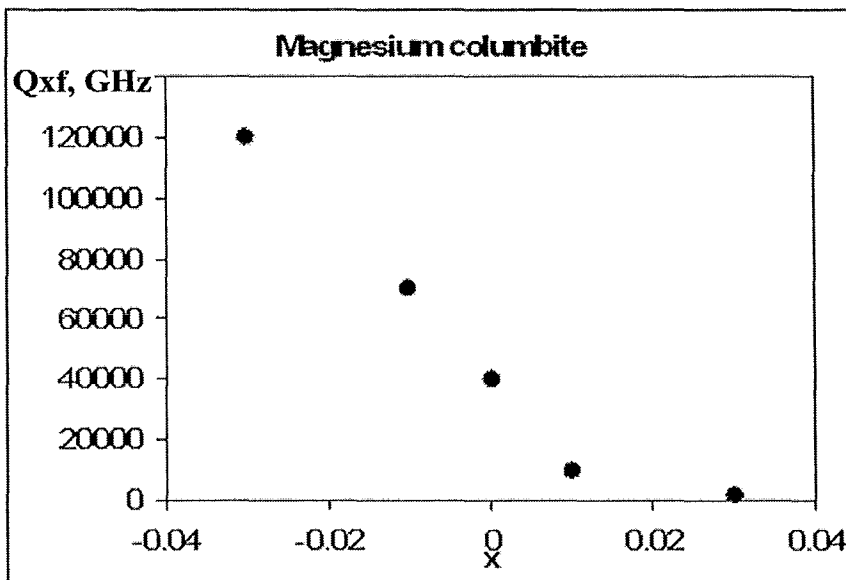


Fig.4.1 Dependence of the quality factor in  $Mg_{1-x}Nb_2O_6$  on the x value (to emphasize the frequency dependence of the quality factor it is common to use Qxf value instead of the quality factor itself)

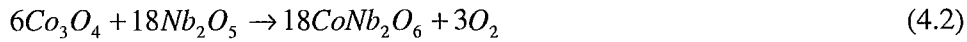
X-ray spectra revealed the presence of  $Nb_2O_5$  for  $x>0$ , the concentration of which smoothly decreases with  $x \rightarrow 0$ , producing a homogeneous region around  $x=0$ . The small value of the quality factor at  $x=0.03$  and  $0.01$  was attributed to the presence of the niobium pentoxide phase [91]. For  $x=-0.03$ , the Q value reaches its maximum. X-ray measurements showed the existence of a  $Mg_4Nb_2O_9$  second phase.  $Mg_4Nb_2O_9$  has corundum structure with higher Q-factor. So, formation of the corundum based phase for  $x=-0.03$  leads to  $Mg_{1.03}Nb_2O_6$  having the highest Qxf value.

The described process of sample preparation is usually accompanied by evaporation of oxygen. In order to compensate for the oxygen loss a set of samples with the same composition was prepared in oxygen atmosphere. Microwave measurements produced Q-values similar to the results obtained on air-sintered samples.

Regarding the values of the temperature coefficient of the resonance frequency and the dielectric constant, they did not change significantly over the used Mg/Nb ratios and had values of -60ppm/k and 20, respectively.

#### 4.1.2 Cobalt Columbite

The reaction describing the formation of cobalt columbite can be written as



The first evidence of  $CoNb_2O_6$  was observed at a sintering temperature of  $600^{\circ}C$  and single phase columbite was obtained in the temperature range  $1100-1150^{\circ}C$ .

Fig.4.2 shows the dependence of the measured Q-values on the chemical composition (Co/Nb ratio) for the samples sintered in air at  $1400^{\circ}C$  for 8 hours.

The value of the Q factor for  $x>0$  is affected by the presence of  $Nb_2O_5$  resulting in it decreasing for the samples with  $x \rightarrow 0.05$ . The decrease of the quality factor in the region of  $x<0$  is because of the presence of a second, Co-rich phase. For  $x=0$  the concentration of that phase is the highest resulting in the maximum of the quality factor.

Measurements of the dielectric constant for stoichiometric and non-stoichiometric samples resulted in the same values as for magnesium columbite. However, contrary to the case of magnesium columbite that had almost constant TCF for all measured x compositions, the TCF for cobalt columbite is slightly lower and varies within samples with different x; from -65 to -80ppm/K.

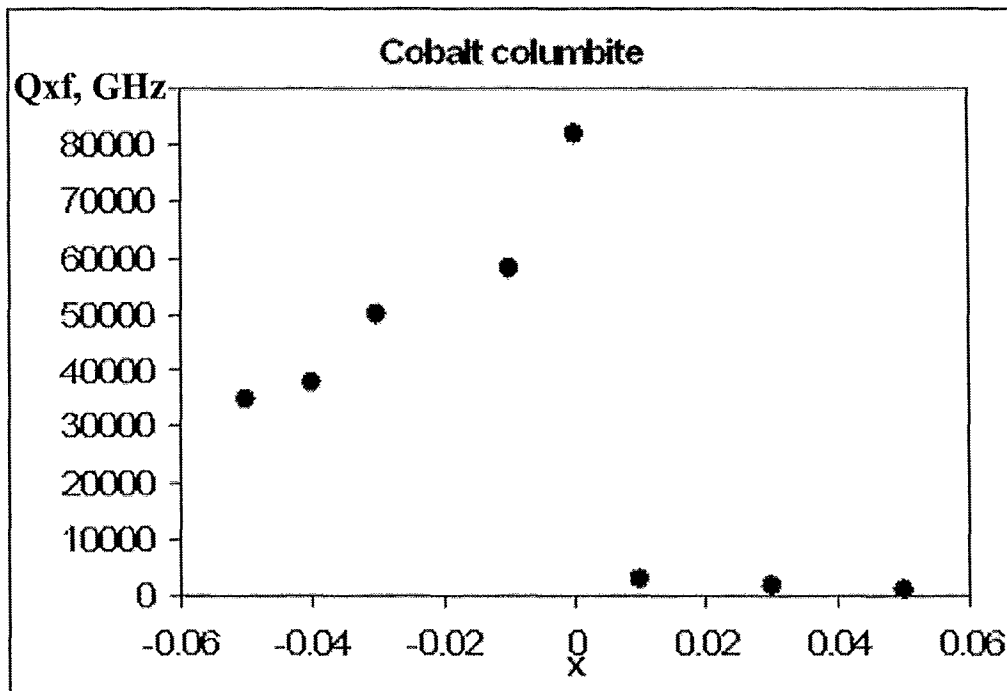


Fig.4.2 Dependence of the quality factor in  $Co_{1-x}Nb_2O_6$  on the x value

#### 4.1.3 Zinc Columbite

The formation of  $Mg_{1-x}Nb_2O_6$  and  $Co_{1-x}Nb_2O_6$  was paralleled by the presence of the second phases over all x values. In contrast to the Mg and Co columbites, the appearance of  $ZnNb_2O_6$  starts at lower temperatures ( $500^\circ C$ ) and proceeds without creation of second phases significantly simplifying the formation of zinc containing columbites.

In the beginning of this chapter it was mentioned that the microwave properties of the final ceramics depended on the presence of the second phases during

the sintering of the columbite type material. So, one would expect that  $Ba_3ZnNb_2O_9$  appears without the presence of any second phases.

The Q-value depends on the density of the material. High temperature sintering of zinc columbite is characterized by zinc evaporation resulting in a densification of the material. Different degrees of densification for different x values result in varying quality factors. Microwave measurements demonstrated that the values of the Qxf product for  $Zn_{1-x}Nb_2O_6$  do not change significantly with changing x values reaching a maximum for x=-0.01 where the probable density of the structure is the largest.

X-ray measurements conducted for different sintering temperatures indicated even higher evaporation of oxygen in comparison with Mg and Co columbites. A series of samples sintered in the presence of oxygen showed an even more flat Qxf(x) dependence (fig.4.3)

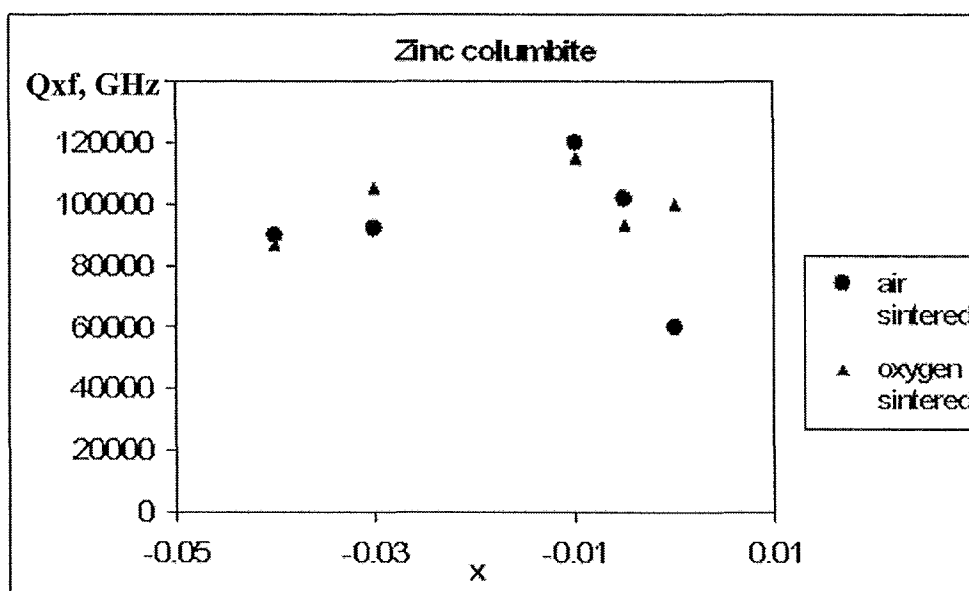


Fig.4.3 Dependence of the quality factor in  $Zn_{1-x}Nb_2O_6$  on the x value

The value of TCF was on the order of -75 ppm/K and does not vary as much as the one for cobalt columbite. The magnitude of the measured dielectric constant was around 22 ÷ 23.

According to the results of microwave measurements some samples exhibiting good values of the quality factor were studied by the positron annihilation technique. In order to reveal an influence of the degree of purity of the initial reagents some samples were produced from the reagents having different levels of impurities:

- a) two sets of samples of magnesium columbite with  $x=0, -0.01, -0.03$  sintered in air and in the presence of oxygen (10 atm) at  $1390^{\circ}\text{C}$  for 8 hours were prepared from high purity Japanese reagents and chemical purity Ukrainian reagents.
- b) samples of cobalt columbite with  $x=0, -0.005, -0.01, -0.03, -0.04$  sintered in air and in the presence of oxygen (10 atm) at  $1380^{\circ}\text{C}$  for 8 hours were prepared from high purity Japanese reagents and chemical purity Ukrainian reagents.
- c) zinc columbite samples with  $x=0, -0.005, -0.01, -0.03, -0.04$  sintered in air and in presence of oxygen (10 atm) at  $1300^{\circ}\text{C}$  for 8 hours were produced from high purity zinc oxide (Aldrich) and Ukrainian chemical purity niobium pentoxide.

## 4.2 Materials with Perovskite Structure

Perovskite type materials  $Ba_3B'Nb_2O_9$  ( $B' = \text{Mg}, \text{Co}$  and  $\text{Zn}$ ) were sintered with different  $B'/\text{Ba}$  and  $B'/\text{Nb}$  ratios at several sintering temperatures.

### 4.2.1 Cobalt Perovskite ( $Ba_3Co_{1+x}Nb_2O_9$ )

A series of perovskites  $Ba_3Co_{1+x}Nb_2O_9$  ( $x = -0.07, -0.04, 0, 0.01, 0.03$ ) were sintered at  $1400^\circ\text{C}$ . The results of X-ray and microwave measurements are summarized in Table 4.1

Table 4.1 Results of X-ray and microwave measurements on  $Ba_3Co_{1+x}Nb_2O_9$  perovskites

x	XRD	Qxf, GHz
-0.07	-weak ordering -Ba-rich phase	84000
-0.04	-no ordering -weak secondary phase	72000
0	-no ordering -weak secondary phase	60000
0.01	-no ordering -weaker secondary phase	60000
0.03	-no ordering -traces of secondary phase	54000

X-ray measurements revealed that deviation from stoichiometry in the B-sublattice is accompanied by the formation of second Ba-rich phases ( $Ba_5Nb_4O_{15}$  and, probably,  $Ba_4Nb_2O_9$ ) and insignificant ordering in the perovskite phase.

The Q-value reaches its maximum at  $x=-0.07$  where according to the X-ray results, the concentration of Ba-rich phases is the highest and there is weak B-site ordering. For all studied samples the dielectric constant was in the range 32-34.

#### 4.2.2 Cobalt Perovskite ( $Ba_{3+3x}CoNb_2O_9$ )

$Ba_{3+3x}CoNb_2O_9$  where  $x=-0.02, -0.01, -0.005, 0, 0.005$  were produced at a slightly higher temperature ( $1445^{\circ}\text{C}$ ). The results of X-ray and microwave measurements are shown in Table 4.2.

Table 4.2 Results of X-ray and microwave measurements on  $Ba_{3+3x}CoNb_2O_9$  perovskites

x	XRD	Qxf, GHz
-0.02	-ordering - $Ba_6CoNb_9O_{30}$	8000
-0.01	-weak ordering - $Ba_6CoNb_9O_{30}$	15000
-0.005	-no ordering - $Ba_6CoNb_9O_{30}$	35000
0	-no ordering -traces of secondary phase	60000
0.005	-no ordering -traces of secondary phase	45000

The changes in the Q-value are the result of two competing processes: small ordering in the perovskite type material that is highest for  $x=-0.02$  and simultaneous formation of the second phase (probably  $Ba_6CoNb_9O_{30}$ ) which also influences the Q-value. For  $x=0$ , where just small traces of the second phase were observed, the Q-

factor reaches its maximum. Evidently, the presence of the second phase in the structure decreases the value of the quality factor of the whole system. Deviation from the stoichiometry does not change the dielectric constant which as in case of BCN samples with cobalt variation was in the range 32-34.

#### **4.2.3 Zinc Perovskite ( $Ba_3Zn_{1+x}Nb_2O_9$ )**

Four samples of zinc perovskite  $Ba_3Zn_{1+x}Nb_2O_9$  ( $x=-0.07, -0.04, 0, 0.005$ ) were prepared at  $1400^{\circ}C$ . The results of X-ray and microwave characterization are summarized in Table 4.3.

Table 4.3 Results of X-ray and microwave measurements on  $Ba_3Zn_{1+x}Nb_2O_9$  perovskites

x	XRD	Qxf, GHz
-0.07	-no ordering	50000
	-second phase	
-0.04	-no ordering	60000
	-second phase	
0	-no ordering	65000
	-second phase	
0.005	-no ordering	50000
	-second phase	

All samples revealed the presence of second phases, which can probably be  $Ba_5Nb_4O_{15}$  and  $Ba_4Nb_2O_9$ , as in the case of cobalt perovskites.

The value of the quality factor is almost constant over the studied range of x. So, even if the second phase influences the quality factor of zinc perovskite, the concentration of the former one does not change significantly over the investigated x

values. For x values equal to 0.01 and higher it was not possible to obtain dense ceramics up to sintering temperatures of 1600°C.

The dielectric constant of BZN samples was slightly higher than that of BCN samples and was within 39-41 range.

#### 4.2.4 Zinc Perovskites ( $Ba_{3+3x}ZnNb_2O_9$ )

$Ba_{3+3x}ZnNb_2O_9$  ( $x=-0.02, -0.005, 0.005$ ) samples were sintered at two different temperatures and the results of XRD and microwave measurements are presented in Table 4.4.

Table 4.4 Results of X-ray and microwave measurements on  $Ba_{3+3x}ZnNb_2O_9$  perovskites

x	XRD	Qxf,GHz
-0.02 (1370C)	-weak ordering - $Ba_6ZnNb_9O_{30}$ (?)	5000
-0.02 (1440C)	-no ordering - $Ba_5Nb_{14}O_{15}$ (?)	92000
-0.005 (1370C)	-weak ordering - $Ba_6ZnNb_9O_{30}$ (?)	20000
-0.005 (1440C)	-no ordering - $Ba_5Nb_{14}O_{15}$ (?)	65000
0.005 (1370C, 1440C)	-no ordering -traces of the second phase	42000

The behavior of the Q-factor versus x-value is different for the samples sintered at different temperatures. The highest Q was obtained for  $x=-0.02$  (1440°C). One of the main differences among the samples sintered at different temperatures is

the formation of two different second phases ( $Ba_5Nb_{14}O_{15}$  for higher and  $Ba_6ZnNb_9O_{30}$  for lower sintering temperatures), which influences the value of the Q-factor.

The value of the dielectric constant was within the range 39-41.

#### **4.2.5 Magnesium Perovskites**

Only samples with negative values of x ( $x=-0.03$ ) and stoichiometric composition could be sintered in the accessible temperature range (up to  $1700^{\circ}\text{C}$ ). For  $x=-0.03$  and 0, sintered at  $1400^{\circ}\text{C}$ , noticeable ordering was observed from the X-ray spectra and the measured quality factors were 35000 and 50000, respectively.

All stoichiometric and non-stoichiometric perovskite type samples described above were studied by positron annihilation spectroscopy (except for the magnesium perovskites, where only the stoichiometric composition was characterized). Because of the specificity in dimensions of the samples, X-ray measurements conducted at McMaster University were not very sensitive to the presence of the second phases. So, some of the measurements performed by Ukrainian colleagues will be used to facilitate an explanation of the data obtained from positron lifetime and Doppler broadening experiments.

# **Chapter 5**

## **Positron Annihilation Experimental Setup**

This chapter contains experimental details of the performed work. The schematic of the positron lifetime setup, followed by a description of the data analysis will be presented at first. Then, the experimental arrangement for the coincidence Doppler broadening measurements as well as the procedure for data interpretation will be given.

### **5.1 Lifetime Spectroscopy**

Positron lifetimes can be detected by measuring the time difference between the 1.27MeV (indicating the birth of positron in the source) and one of the annihilation 511keV  $\gamma$ -quanta. A schematic of the PLS experimental setup used in this work is given in fig.5.1.

The source of positrons ( $^{22}Na$ ) is sandwiched between two identical samples to ensure annihilation of all positrons inside of the studied material. By using samples that are thick enough one guarantees that all annihilation occurs in the material of the samples (in our case the thickness of the samples was not less than 2mm). Once a positron enters the sample it eventually annihilates producing  $\gamma$ -quanta. Plastic scintillators, detecting the  $\gamma$ -quanta, emit light that is converted into an electrical signal by photomultiplier tubes.

The amplitude of the output pulses from the scintillator-photomultiplier assembly is proportional to the energy of the incident  $\gamma$ -quanta. Constant Fraction

Differential Discriminators (CFDD) are used to discriminate between signals originating from gamma rays with different energies. One of the CFDDs gives a signal after detection of a 1.27MeV gamma ray (that serves as a start pulse for Time-To-Amplitude Conversion (TAC) block). The second

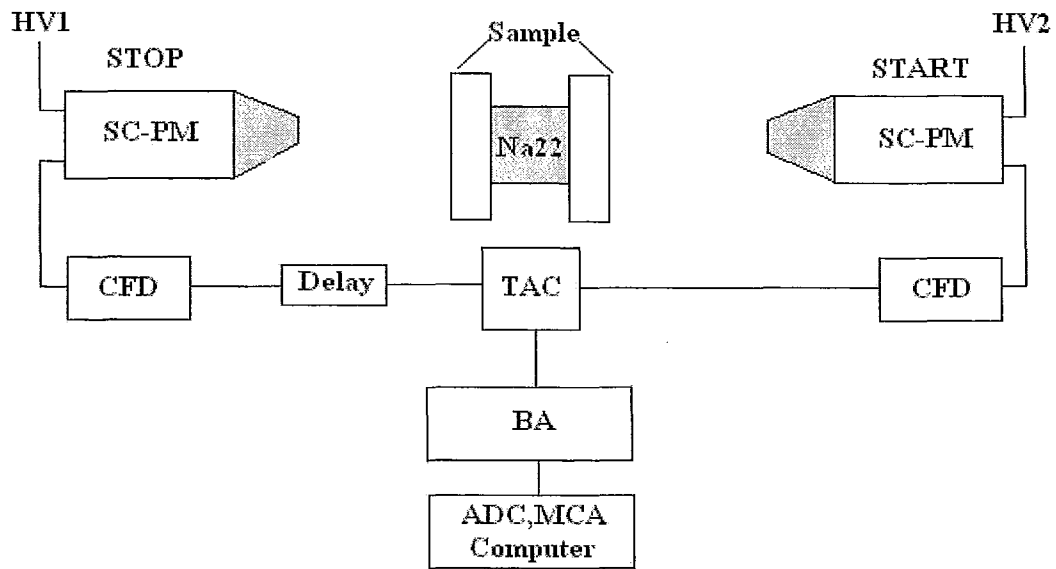


Fig.5.1 Positron Lifetime Experimental Setup

HV	(high-voltage power supply)
SC-PM	(scintillator photomultiplier assembly)
CFDD	(constant fraction discriminator)
TAC	(time-to-amplitude converter)
Delay	(delay line)
BA	(biased amplifier)
ADC	(analog-to-digital converter)
MCA	(multichannel analyzer)

CFDD triggers a stop signal after detection of a 511keV  $\gamma$ -quantum. The amplitude of the pulse on the output of the TAC is proportional to the time difference between the “birth” of the positron and its annihilation. Because of nonlinear transmission

characteristics of the TAC, a delay circuit is introduced into the system to shift the TAC in the linear operation range.

The analog signal proportional to the lifetime of the positron in the material is converted into logical pulses by an analog-to-digital converter and then stored in the memory of a multi-channel analyzer.

## 5.2 Interpretation of Lifetime Spectra

Since the response time of photomultiplier tubes and all accompanying electronics is finite, the spectrum on the output of the MCA contains signals from the annihilation events modified by the resolution of the experimental setup. The measured spectrum is the convolution of the lifetime spectrum with the resolution function of the instrument:

$$S(t) = A \times \{R(t) \otimes [\sum_{i=1}^n \frac{I_i}{\tau_i} \exp(-\frac{t}{\tau_i})]\} \times \Delta t + B \quad (5.1)$$

Here,  $A$  is the total number of counts in the spectrum,  $R(t)$  is the resolution function of the system,  $\Delta t$  is the time difference between two consecutive channels in the MCA,  $B$  is the background signal,  $\tau_i$  is the  $i$ -th lifetime component in the spectrum with the intensity  $I_i$  and  $t$  denotes time.

After deconvolution of (5.1) and background subtraction, the spectrum from the annihilation events can be presented as

$$N(t) = \sum_{i=1}^{k+1} \frac{I_i}{\tau_i} \exp(-\frac{t}{\tau_i}) \quad (5.2)$$

The number of components in (5.2) is, basically, limited by the resolution function of the experimental setup. In practice one can usually separate up to four components.

The resolution of our system is on the order of 230psec. Relatively low resolution results in inability to distinguish components in lifetime spectrum that are closer than 50psec from each other.

For the present research the standard computer program PATFIT88 [92] was used to process the spectra. It automatically performs deconvolution of the spectrum, background subtraction and source correction.

### 5.3 Doppler Broadening Spectroscopy

The schematic of setup used for measuring the Doppler broadened annihilation line in a coincidence configuration is shown in fig.5.2.

Two high purity germanium detectors were positioned collinearly at a distance 40cm from each other. A positron source with activity of  $20\mu Ci$  was sandwiched between two identical samples in the middle of detectors' system. The annihilation events result in simultaneous emission of a pair of  $\gamma$ -quanta at  $\approx 180^\circ$  to each other. Both of the gamma quanta strike the surface of the detectors almost simultaneously inducing electron-hole pairs that are separated by an applied high voltage (2900V).

After amplification, a signal proportional to the energy of an incident gamma quantum is fed into an analog-to-digital converter. One of the detectors is used to create an "input" signal and the second one is to give a "trigger" pulse. The resolution of the first detector should be high enough to detect any changes in the Doppler

broadened line (1.8keV for the detector used in present configuration; resolution was measured at 1.33MeV).

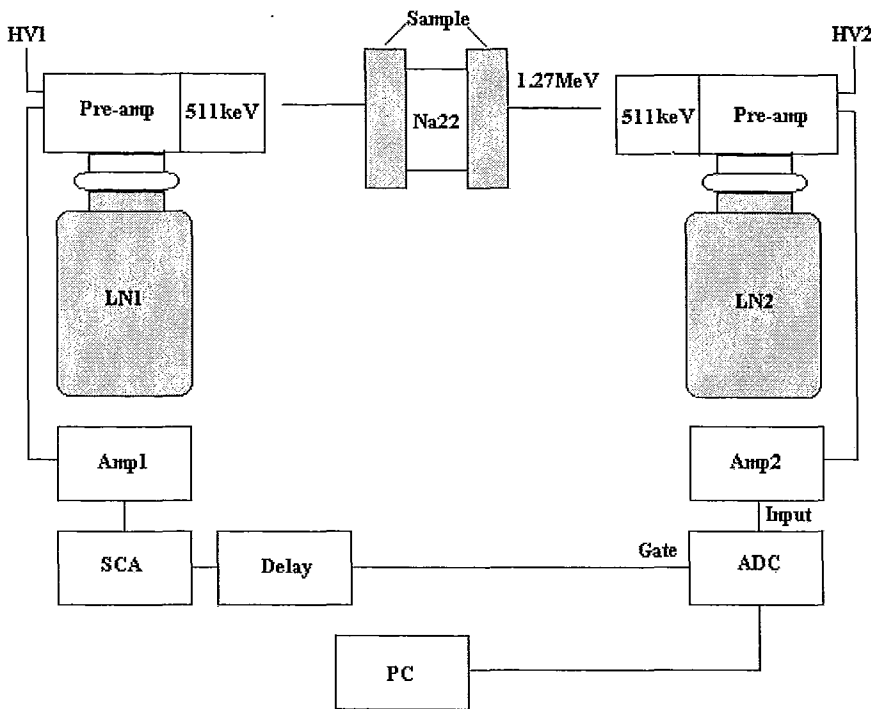


Fig.5.2 Coincidence Doppler Broadening Setup

Pre-amp	(germanium detector with built in preamplifier)
HV	(high-voltage power supply)
LN	(dewar with liquid nitrogen)
Amp1	(amplifier)
Amp2	(amplifier)
SCA	(single channel analyzer)
Delay	(delay line)
ADC	(analog-to-digital converter with stabilizer)

At the same time, the resolution of the second detector does not influence significantly the final results.

In one of the arms a single channel analyzer is introduced in the system in order to differentiate the 511keV signals.

Pulses from the output of the ADC appear only when “input” and “gate” signals are present simultaneously at the input of ADC. This ensures that only pulses originating from the same annihilation events will be detected. To equalize the time that the signals travel from both detectors to the ADC, a delay line is used in the system.

After acquisition, the digital signal was stored in a multi-channel analyzer and processed by Genie-2000 software, a Canberra product.

The settings of the amplifier and ADC were adjusted to give an energy dispersion of about 75eV per channel. Each spectrum contained one million counts giving around 20 000 counts in the peak channel.

## 5.4 S and W Parameters

An example of the experimental Doppler spectrum  $N_D = f(E)$  obtained in the present work is shown in fig.5.3 and a description of the so-called SW-technique, that is commonly used for the analysis of the Doppler broadened annihilation line is presented below [56].

The S-parameter (sometimes called valence annihilation parameter) describes the narrowness of the annihilation line and is defined as the ratio of counts in the central part of the Doppler broadened spectrum to the total number of counts:

$$S = \frac{\int_{E_0-E_S}^{E_0+E_S} N_D dE}{\int_{-\infty}^{+\infty} N_D dE} \quad (5.3)$$

The W-parameter is defined as the ratio of counts in one of the “wings” of the annihilation line to the total number of counts:

$$W = \frac{\int_{E_1}^{E_2} N_D dE}{\int_{-\infty}^{+\infty} N_D dE} \quad (5.4)$$

For the S value, the interval limits are chosen symmetrically around the 511keV peak value. For the W parameter, the energy values  $E_1$  and  $E_2$  should be chosen so as to have no correlation with the S parameter. They should be kept constant for all spectra to be compared. Different authors, however, define S and W parameters in different ways. So, it is not possible to compare absolute values of S and W parameters obtained from different groups.

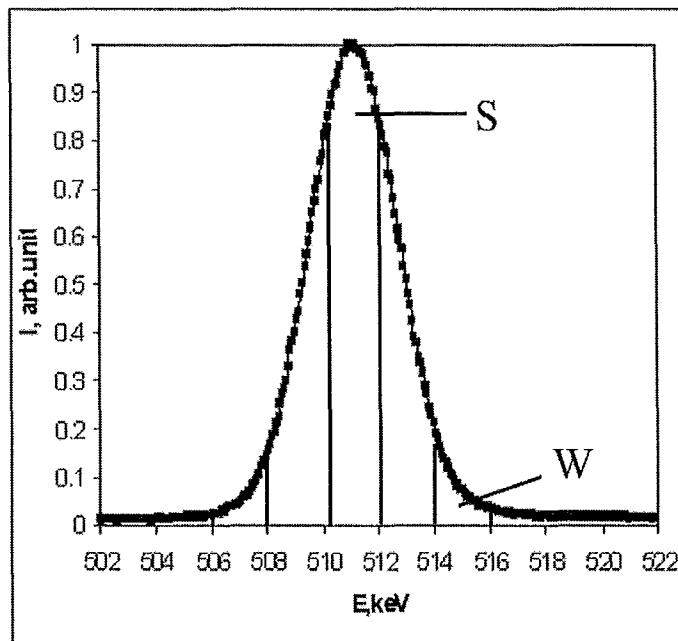


Fig.5.3 Experimental Doppler broadened Annihilation Line

The shape of an S *versus* W curve depends on the number of different types of defects present in the sample. For a sample with only one type of defect, the S *versus*

W dependence is linear [56]. In case of two or more defects, the S-W curve is more complicated.

For the calculation of the S parameter, the value of  $E_s = (511 \pm 1)keV$  was chosen and for the W parameter values of  $E_1 = 514keV$  and  $E_2 = 518keV$  were used.

## Chapter 6

### Experimental Results and Their Discussion

This chapter deals with the explanation of the results obtained on columbite and perovskite type materials by means of lifetime and Doppler broadening spectroscopy. Theoretical calculations of the bulk lifetime for the studied specimens were done by using the MIKA package obtained from Helsinki University of Technology [93].

#### 6.1 Columbite Materials

Positron lifetime spectra of  $A_{1+x}Nb_2O_6$  ( $A=Mg, Co, Zn$  and  $x=0 \div 0.05$ ) samples were decomposed into 3 components. As will be shown later in this section, the first component is the so called “reduced bulk lifetime” with values lower than the bulk lifetime. The second component originates from positrons annihilating in defects. The last, third lifetime, having values around 2nsec was attributed to annihilations on the surface of the samples. The third lifetime was not of practical interest for the given studies and is omitted in the discussion. Table 6.1 contains the lifetime components and their intensities for some of the stoichiometric samples used in the present work and Fig.6.1a,b, and c show the dependence of the first lifetime component on the x-value for Mg, Co and Zn samples sintered in air. For the  $Mg_{1+x}Nb_2O_6$  and  $Zn_{1+x}Nb_2O_6$  columbites the value of this component is longer (around 172psec).

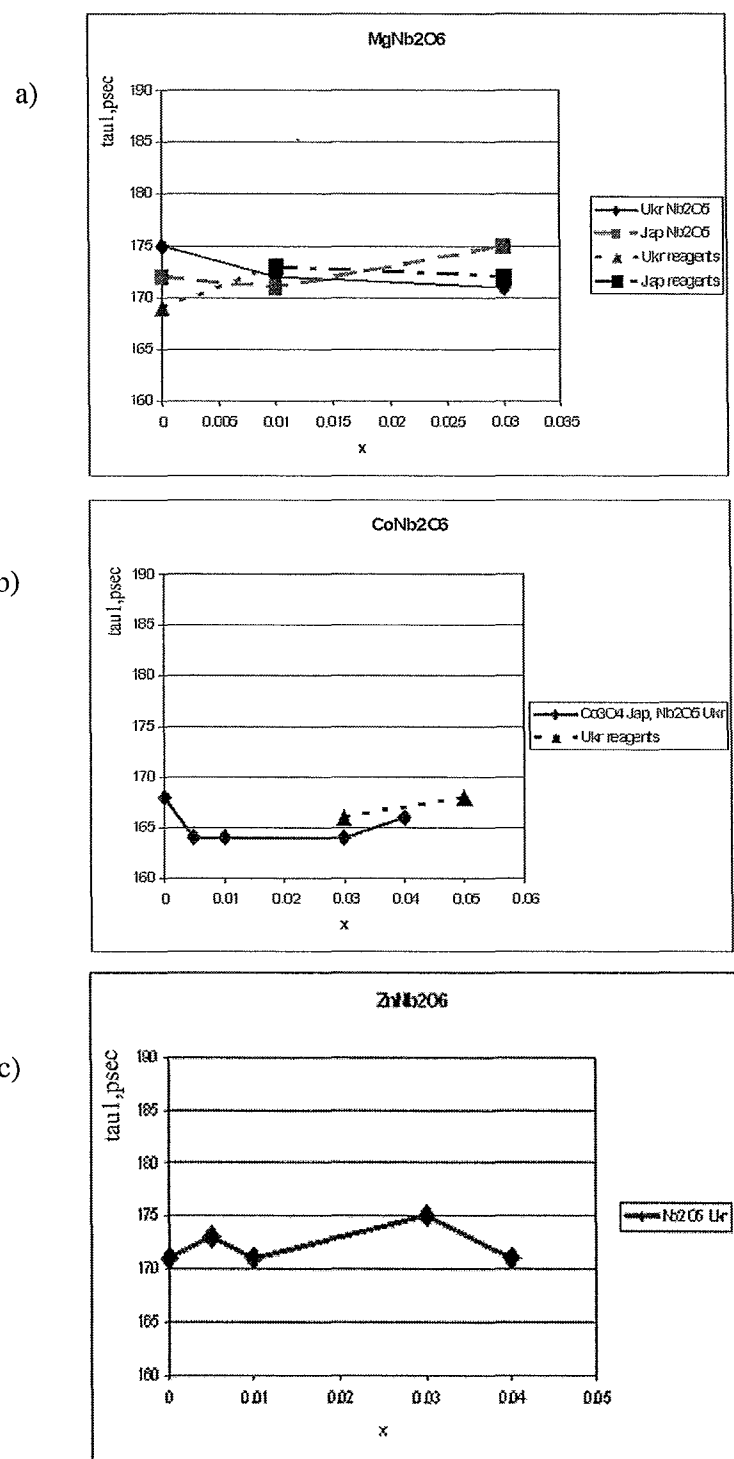


Fig.6.1 Dependence of the first lifetime component,  $\tau_i$ , on the x value (the lines are guides to the eye only)

Table 6.1 Decomposed components for stoichiometric columbites

Material	$\tau_1, p\text{ sec}$	$\tau_2, p\text{ sec}$	$I_1, \%$	$I_2, \%$
$MgNb_2O_6$	$173 \pm 0.5$	$365 \pm 17$	$90 \pm 0.7$	$8.3 \pm 0.6$
$CoNb_2O_6$	$167 \pm 0.5$	$412 \pm 20$	$95 \pm 0.5$	$3.5 \pm 0.4$
$ZnNb_2O_6$	$172 \pm 0.5$	$392 \pm 15$	$93 \pm 0.5$	$5.4 \pm 0.5$

The intensity of the first lifetime component is more than 90% and is slightly smaller for the  $Mg_{1+x}Nb_2O_6$  columbites (90-94%) versus 94-95% for cobalt and zinc columbites. The high value of the intensity of the first component indicates that either almost all positron annihilation occurs inside of the bulk of the media or the first lifetime value represents the superposition of two or more lifetime components that have to be resolved. In the first case the first lifetime component represents the value close to the bulk lifetime and can be used to characterize the material. Otherwise additional lifetime measurements involving the collection of a much larger number of counts would have to be done, to allow further decomposition of the spectra (in the present work 6 million counts were collected for each spectrum).

The values of the second lifetime component for all samples are more than two times larger than those for the first one and range within 360-450 psec. The intensities of the second component are higher for magnesium columbite (5.3-8.3%) and almost equal for the cobalt and zinc columbites (3.5-5.5%).

In order to answer the above questions, first a comparison of the first lifetime component to the theoretical values has to be performed.

For the calculation of the bulk as well as defect lifetimes the MIKA package was used. This program requires entering of atomic positions to calculate the positron wavefunction. The crystal lattice was constructed involving roughly 300 atoms for

each structure. The values of the lattice constants were adapted from the literature [94-96]. The results of the theoretical simulations together with the dimensions of the unit cell are presented in Table 6.2

Table 6.2 Results of theoretical calculations of the bulk and defect lifetimes in columbite type materials by using Boronski-Nieminen enhancement factors within the Linear Density Approximation (LDA) and Arponen-Pajanne enhancement factors within the Generalized Gradient Approximation (GGA).

Boronski-Nieminen enhancement factor, LDA			
	$MgNb_2O_6$	$ZnNb_2O_6$	$CoNb_2O_6$
tau_bulk, psec	150.7	147.1	145.7
O_vacancy, psec	152.6	147.4	147.1
A_vacancy, psec	183.9	179.7	181.6
Nb_vacancy, psec	175.1	172.0	172.2
Arponen-Pajanne enhancement factor, GGA			
tau_bulk, psec	177.4	176.6	172.7
O_vacancy, psec	180.7	177.2	174.9
A_vacancy, psec	228.6	223.0	226.1
Nb_vacancy, psec	218.6	215.6	214.9
a, Å	14.1875	14.208	14.1475
b, Å	5.7001	5.726	5.7120
c, Å	5.0331	5.04	5.0446

The first part of the Table 6.2 contains bulk and defect lifetimes calculated by using the Boronski-Nieminen enhancement factor within LDA approximation. As was mentioned in the part devoted to the background of the theoretical simulations, an application of the LDA for the “electron-positron” screening problem overestimates annihilation rates and hence gives low lifetime values. In the given case of three materials having the same symmetry and close lattice constants, calculations with the BN enhancement factor within LDA give trends for the values of the bulk lifetimes:

$MgNb_2O_6$  exhibits the largest bulk value, which decreases for the zinc compound and reaches a minimum for the cobalt columbites.

For oxygen vacancies, simulations resulted in lifetime values close to the bulk one. This shows an insensitivity of the positrons to the presence of oxygen defects. For missing A-type (A=Mg,Zn and Co) or Nb atoms the calculations give lifetimes that are roughly 33 and 25 psec longer than the bulk values, respectively. The fact that defect lifetimes are “far” from the bulk values indicates the presence of the attractive potential for the positrons created by missing atoms and results in positrons becoming trapped in the given vacancies.

Positron density distributions for O-, A-, and Nb- type defects are presented in Fig.6.2 They confirm the inability of positrons to reveal the presence of oxygen defects in the given columbite materials and positron localization (trapping) in metal vacancies.

The second part of Table 6.2 contains positron lifetimes obtained by employing Arponen-Pajanne (AP) enhancement factors within GGA. In comparison to the BN enhancement factors, application of AP produces longer bulk and defect lifetimes while preserving the trend from magnesium, to zinc and cobalt columbites. Again, simulations of the columbites containing oxygen defects show inability of positrons to detect oxygen vacancies.

Returning back to the decomposed experimental spectra one can see that the first lifetime component is quite close to the values calculated by using the AP enhancement factor. So, it is possible to conclude that  $\tau_1$  represents the reduced bulk value with intensities of more than 90% rather than a superposition of several

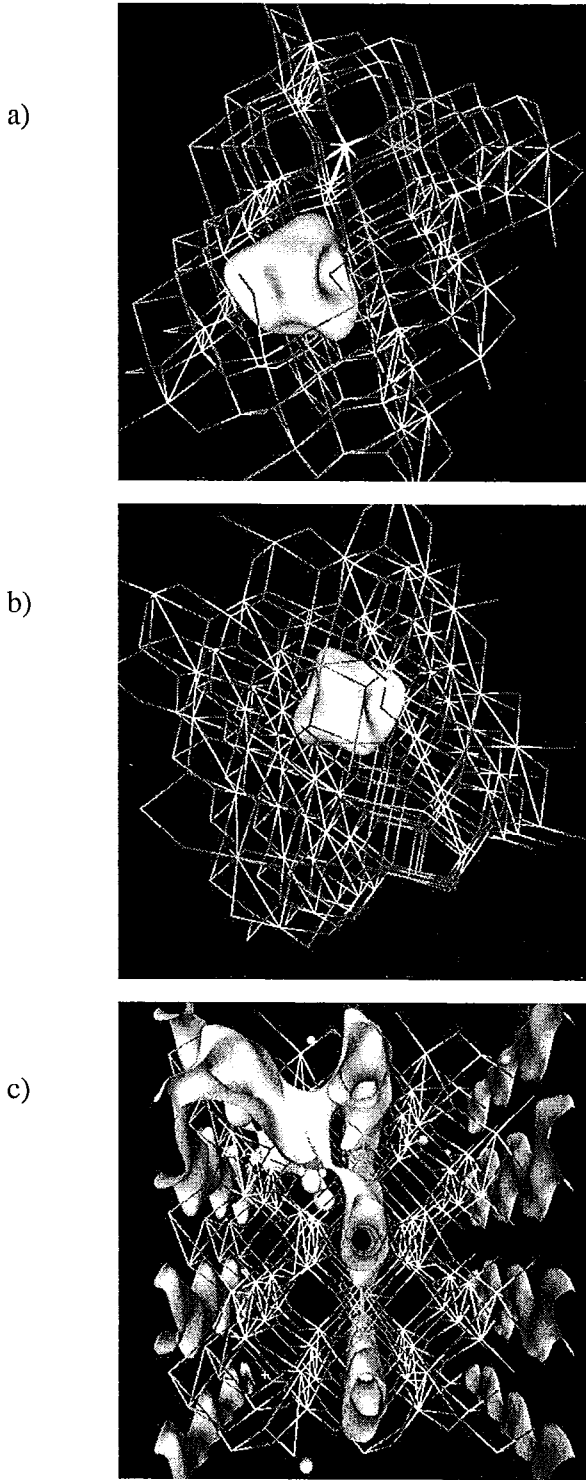


Fig.6.2 Positron density distribution in columbite type materials in case of a) A-vacancy ( $A=Mg, Zn$ , or  $Co$ ), b) Nb-vacancy, c) O-vacancy

unresolved components. Now the question is: "what is the origin of the second lifetime component with quite low intensity?"

As one can see the calculated defect lifetimes vary within 215-230 psec. At the same time experiments show the presence of defects with lifetimes in the range 360-450 psec. Any attempts to calculate lifetimes in defect clusters representing two or more missing atoms resulted in lifetime values much shorter than those from the experiment.

The preparation of the samples involved mixing of powders of corresponding oxides with the powder of niobium pentoxide. After firing, the samples had grained structures which can be perfect positron traps. According to the Monte-Carlo simulations of Hubner *et al* [90] on grained materials the fraction of positrons annihilating inside of the grain boundaries depends on the diameter of the particles.

The size of the particles in the studied samples was estimated by using reflection optical microscopy. Images taken from the optical microscope are shown in Fig.6.3a,b and c. All recordings were done under the same magnification of the microscope. So, one can compare how the size of the grains changes from one material to the other.

The image of the surface of magnesium columbite is presented in fig.6.3a. The mean diameter of the grains is around  $2\text{-}5 \mu\text{m}$ . For zinc and cobalt columbites (fig.6.3b and c, respectively) the average particle diameter is slightly larger and varies within  $5\text{-}10 \mu\text{m}$ . Simulations of Hubner show (see fig.3.6) that for the given particles' sizes the fraction of the positrons reaching the grain boundaries with subsequent annihilation should be around 10% for the magnesium compounds and roughly 5% for the zinc and cobalt columbites. By looking at Table 6.1 containing intensities of

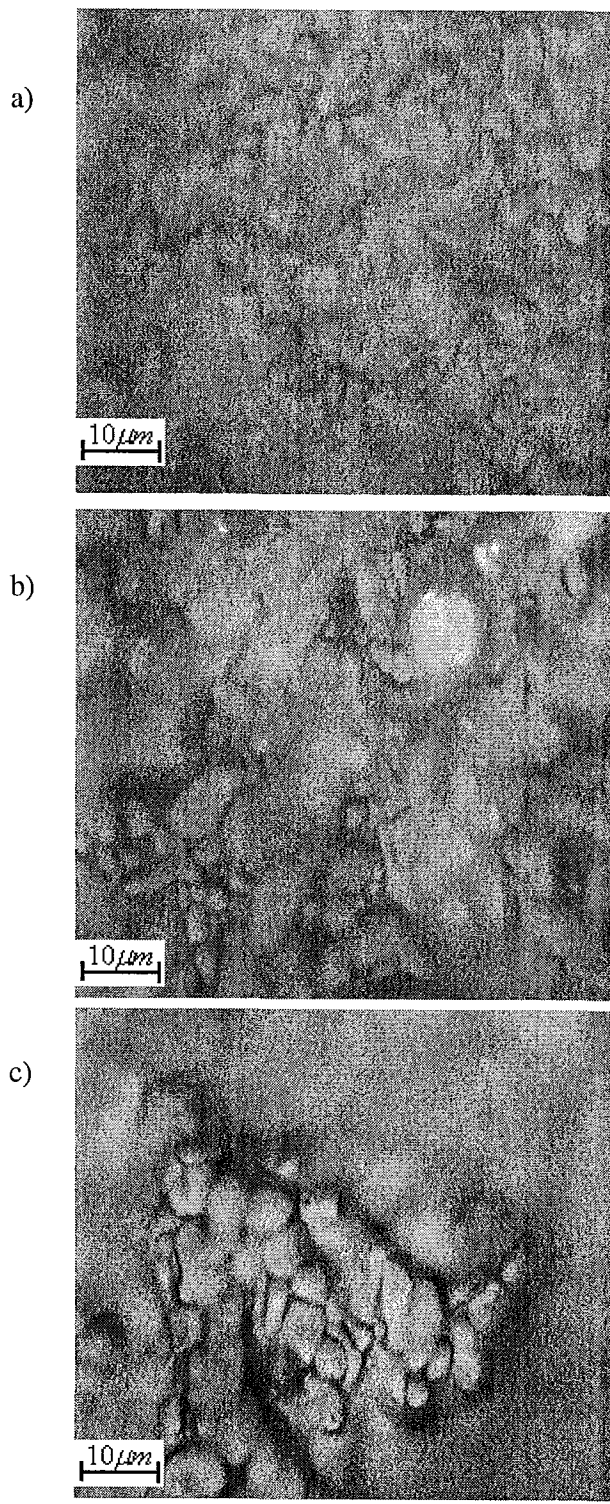


Fig.6.3 Results of reflection microscopy measurements. a)  $MgNb_2O_6$ , b)  $ZnNb_2O_6$ , c)  $CoNb_2O_6$

the second lifetime components one can see strong similarities between the fraction of positrons annihilating inside of the grains and the intensities of the components originating from the annihilation in defects. Thus, one can conclude that the second lifetime component arises because of the annihilation between the grains with the lifetime values varying in a relatively broad range. Even by looking at the images of  $ANb_2O_6$  ( $A=Mg, Zn$  and  $Co$ ) it is possible to see that the thickness of the grain boundary regions is not homogeneous from sample to sample. Different thicknesses of the space between particles result in different defect values. In the present studies the dependence of the defect lifetime on the distance between grains was not studied because of the limited number of available samples.

So, the decomposed experimental spectra consist of the reduced bulk lifetime and a component arising due to positrons reaching grain surfaces. Any attempts to reveal additional components originating from the annihilation in A- or Nb-vacancies ( $\tau = 215 \div 230 \text{ p sec}$ ) or their agglomerates that could be present inside of the bulk of the grains did not succeed. This can be because of two reasons:

- a) either the concentration of the possible defects inside of the grains is so small that positrons are simply insensitive to detect them
- b) the difference between the A- and Nb-vacancy lifetimes and that in the bulk is on the order of or less than 50psec. In order to distinguish such closely separated lifetime values one needs to use spectrometers with very high resolution. So, possibly because of the resolution of the system used in present work, we could not reveal any evidence of the defects inside of the grains.

Having only one defect type, it is possible to use the one defect trapping model described in Chapter 3. The results of the application of the trapping model for  $A_{1+x}Nb_2O_6$  samples (A=Mg,Zn,Co) are presented in fig.6.4 as a function of x.

The value of  $\tau_b$  for all three materials does not vary significantly with x. The results of the Ukrainian colleagues demonstrated that the Q-factor is not constant and peaks because of the presence of the second phases for the magnesium and cobalt columbites and shrinkage of the unit cell in the zinc columbite.

According to the microwave and X-ray measurements conducted by the Ukrainian group, the high value of the quality factor in Mg and Co containing samples appears because of the presence of  $Mg_4Nb_2O_9$  in magnesium columbite and similar compounds in cobalt columbite having corundum structure.

Theoretical simulations of the positron bulk lifetime in  $Mg_4Nb_2O_9$  (dimensions of the unit cell as well as the symmetry of the structure used to construct the supercell for subsequent simulations were taken from reference [97]) resulted in  $\tau_b = 184 \text{ psec}$ . The value of this lifetime is quite close to the one in magnesium columbite (184psec versus 177psec). So, the presence of a small concentration of the second phase would not appreciably change the bulk lifetime of the whole material.

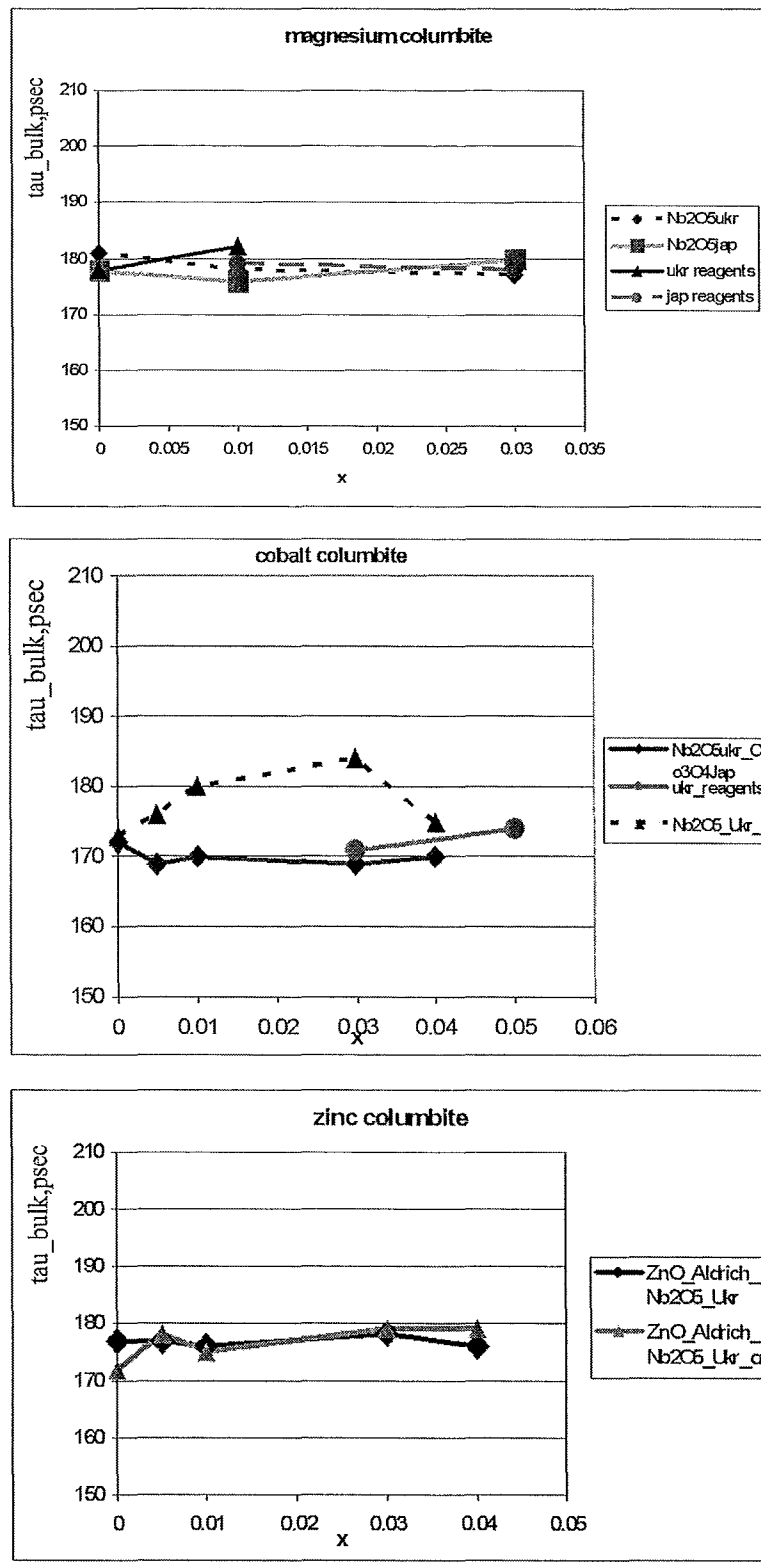


Fig.6.4 Dependence of bulk lifetimes in  $A_{1+x}\text{Nb}_2\text{O}_6$  columbites on  $x$  value (Lines are just guides to the eye)

As for the  $CoNb_2O_6$  samples, unfortunately there are no X-ray data for the  $Co_4Nb_2O_9$  structure in the literature that can be used for the calculation of the bulk lifetime. But by analogy to the calculation conducted for columbite materials, the bulk lifetime of  $Co_4Nb_2O_9$  should be shorter than that for  $Mg_4Nb_2O_9$  and close to the bulk lifetime of the host material  $CoNb_2O_6$ . Again, small concentrations of the  $Co_4Nb_2O_9$  second phase do not allow for positron lifetime measurements to detect them.

From this point of view, the positron lifetime technique has a drawback and fails in detecting the presence of compounds with lifetimes similar to the value in the host material.

Finally, the changes in the Q-factor of the zinc columbites that were attributed to the unit cell shrinkage are not consistent with the results of the lifetime measurements. Since the bulk lifetime is the characteristic parameter of the given material and depends on the dimensions of the unit cell, any deviations in the values of the lattice constants would result in the varying values of the bulk lifetime.

Up to now only samples sintered in air were considered. Some stoichiometric and nonstoichiometric Mg, Zn and Co columbite samples sintered in the presence of oxygen were measured by positron lifetime technique.

The experimental lifetime spectra were decomposed into three components. The most interesting difference in the decomposed spectra for the samples sintered in the presence of air and oxygen is the change in the intensity of the second component associated with the annihilations at the grain boundaries.

Observations made by using a reflection optical microscopy demonstrated an increase in the grain size and the appearance of voids inside of the bulk of the grains.

Voids and grain boundaries represent indistinguishable traps for positrons. The combination of the fraction of positrons annihilating in the space between the particles (which according to the Hubner's simulations should be less than for the samples sintered in air) and inside the voids results in higher intensities of the component originating from the presence of the defects.

As was mentioned in the section describing the samples' preparation conditions all samples (sintered in air and oxygen atmospheres) were fired at the same temperatures. Sintering in an oxygen atmosphere resulted in an increase of the oxidation state of the compound. Generally, materials with higher oxidation states have lower melting points. So, the melting point of  $A_{1+x}Nb_2O_{6+\delta}$  ( $\delta > 0$ , sintered in oxygen) is lower than that of  $A_{1+x}Nb_2O_6$  (sintered in the presence of air). This caused void formation during the sintering of the samples.

The trapping coefficient introduced in Chapter 3 by formula (3.12) was calculated for all three columbite type materials for different x values and is presented in fig.6.5a,b and c. As one would expect, the increase in the intensity of the lifetime originating from the presence of defects resulted in higher trapping coefficients for the samples fired in oxygen.

In order to reveal the possible presence of other defectes inside of the studied specimens, coincidence Doppler broadening measurements were performed and their results are presented in fig.6.6 as a S-W-curve. The dependence of the S parameter on W is linear, implying the existence of only one type of defect - grain boundaries.

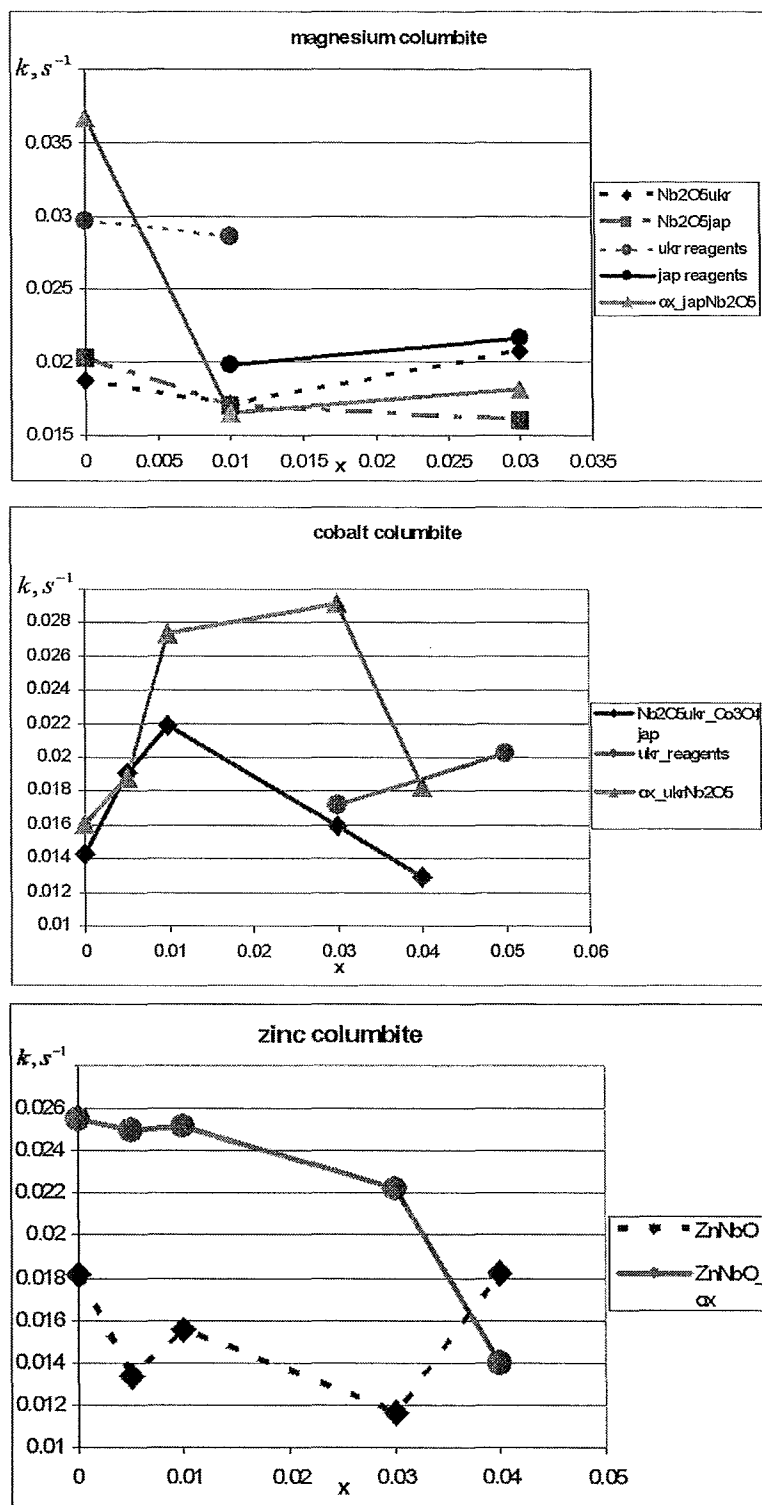


Fig.6.5 Dependence of trapping coefficient on x value for columbite type materials

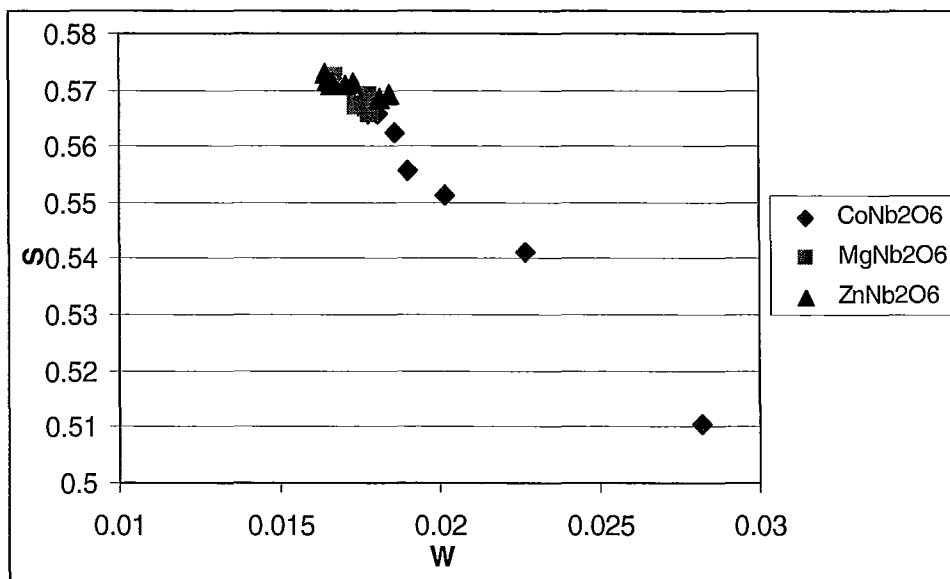


Fig.6.6 SW-plot for columbite type materials

As a summary, lifetime and coincidence Doppler broadening techniques revealed the existence of a single type of defect in the form of grain boundaries that allowed application of the one defect trapping model. The intensity of defect's lifetime component varies depending on the size of the grains. Detection of the second phases was hampered because of the similarities in the bulk lifetime of the impurities and that of the host material.

## 6.2 Positron Annihilation Spectroscopy of Perovskite Samples

All spectra from positron lifetime annihilation experiments were decomposed into three components. In analogy to the columbite samples, the last component with intensities less than 1% was attributed to annihilations on the surface of the samples. The second component with intensities ranging from 24% to 40% for different

samples and lifetimes around 300 psec arises because of annihilations at the grain boundaries. In order to confirm this, a set of microscopy measurements were performed on several samples. The result of one of them is presented in fig.6.7. It was estimated that the diameter of the grains varies from roughly  $0.5 \mu m$  to  $1 \mu m$ . According to Hubner's simulations, 28-40% of positrons would reach grain boundaries with their subsequent trapping and annihilation in materials with particle sizes  $0.5 \div 1 \mu m$  [90].

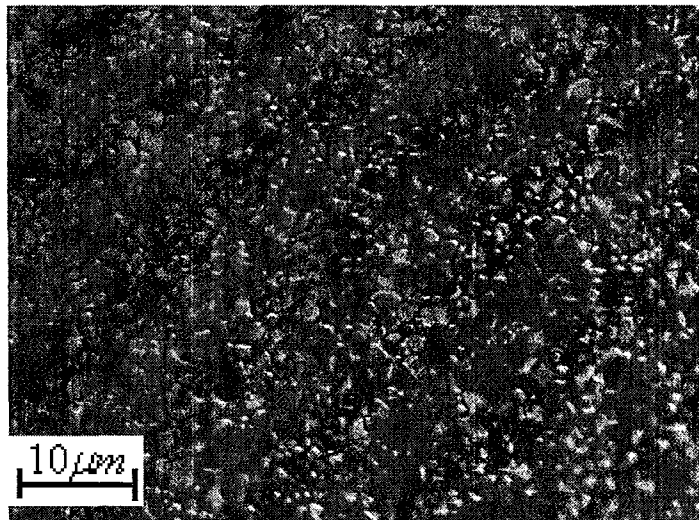


Fig.6.7 Grained surface of perovskite type material

Contrary to the columbite samples, where the scatter in the values of the second lifetime component is quite large ( $\tau_2 = 360 \div 450 \text{ p sec}$ ), for perovskite type materials the change in the value of the second component is insignificant ( $\tau_{\max} - \tau_{\min} \approx 20 \text{ p sec}$ ). This fact can be possibly attributed to a decrease of the particle diameters that creates a more homogeneous distribution of defects (grain boundaries) within the samples.

Any attempts to resolve additional components in the recorded spectra did not succeed. This can again be because of the resolution of the apparatus that does not

allow separation of closely spaced components or low levels of defect concentrations.

In any case, the separation of only one defect component resulting from homogeneously distributed trapping centers justifies the application of the one defect trapping model.

All subsequent sections contain the results of the application of the one defect trapping model to the experimental spectra.

### **6.2.1 $Ba_3MgNb_2O_9$ Sample**

Because of difficulties in the sintering process of nonstoichiometric magnesium perovskites (samples of magnesium perovskite with excess magnesium could not be sintered up to  $1700^{\circ}C$ ) only stoichiometric compositions were prepared and studied by the positron annihilation technique.

Application of the one defect trapping model resulted in  $\tau_b = 204\text{ psec}$ . According to the theoretical calculations of Ghosh [83] on perovskite type materials, the bulk lifetimes for  $LaCoO_3$ ,  $PbTiO_3$  and  $BaTiO_3$  used in her work are 129psec, 147psec and 152psec, respectively. Obviously, they are too far from the experimental bulk lifetimes obtained in the present studies and can not explain our results.

Ghosh's simulations concentrated on the determination of the bulk lifetime of perovskites with one type of atom on the B-sublattice and for this kind of materials her simulations gave outstanding results. But a number of papers involving positron studies on materials with two cations on the B-site produced bulk lifetimes that could not be explained by Ghosh's theory [88,98]. This made us perform our own theoretical simulations for the studied perovskites.

Since preliminary results of Ukrainian colleagues demonstrated small ordering in perovskite samples it would be reasonable at first to estimate the concentration of the hexagonal phase.

The X-ray spectra obtained at McMaster University after subsequent fitting showed the presence of approximately 92% of the cubic phase and 8% of the hexagonal phase in a  $Ba_3MgNb_2O_9$  sample. This is in agreement with the studies of Janaswamy [51] who obtained roughly 7.9% of the hexagonal phase for the firing temperature of 1400 °C (if one recalls that 1400 °C temperature was used to prepare the given sample). Below is shown the experimental X-ray spectrum (fig.6.8). The lattice constants of cubic and hexagonal magnesium perovskite obtained after fitting are as follows:

-cubic phase                     $a=b=c=4.0855\text{\AA}$

-hexagonal phase                 $a=b=5.7871\text{\AA}$                  $c=7.0674\text{\AA}$

Application of these lattice parameters to the calculation of the bulk lifetimes resulted in 194.9 psec for the cubic magnesium perovskite and 237.1 psec for the hexagonal one. Again, as in case of the columbite samples, the calculation of the bulk lifetime for the magnesium perovskite as well as lifetimes of cobalt and zinc perovskites were done by using the generalized gradient approximation ( $\alpha = 0.22$ ) and an Arponen-Pajanne enhancement factor.

As one can see, the change in the lattice structure significantly influences the positron results. A mixture of roughly 92% of the cubic phase and the rest of the hexagonal phase should produce an “average” bulk lifetime of around 200 psec. This is very close to the experimental value of 204 psec. Small differences can arise either

because of the possible presence of impurities which increase the bulk lifetime of the whole material or because of the accuracy of the method used in the calculations.

The discrepancies between lifetimes in the ordered and disordered structures (237psec versus 195psec, respectively) can be used to evaluate the degree of the B-site cation ordering in BMN perovskites in the absence of second phases.

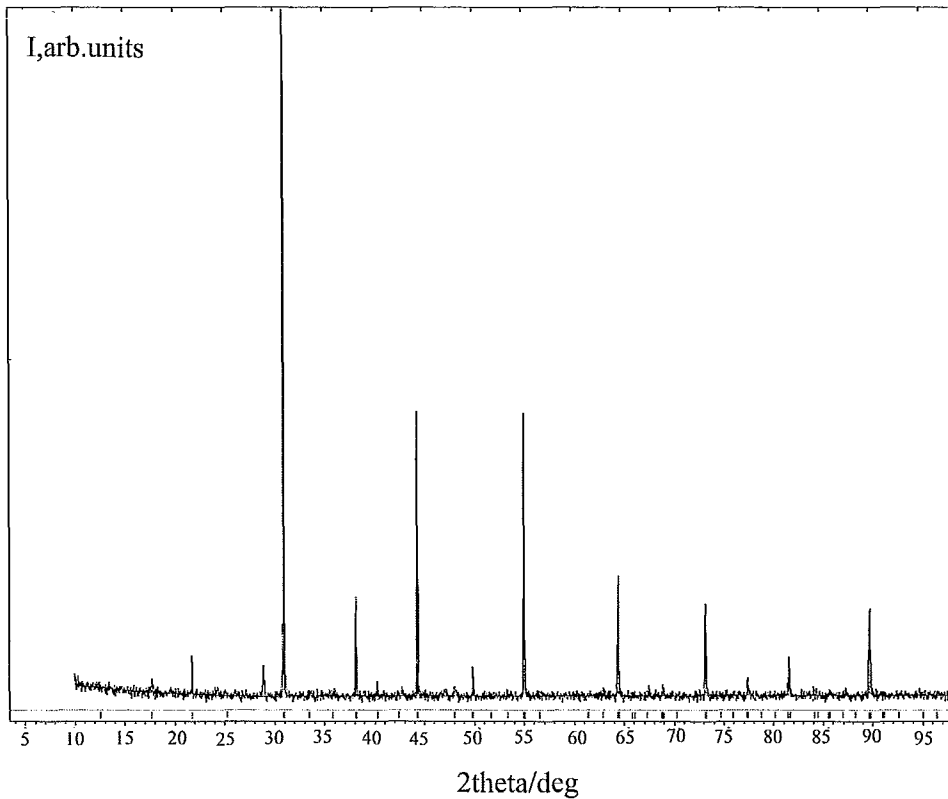


Fig.6.8 X-ray diffraction spectrum for a magnesium niobium perovskite sample

Again, by looking back on the results of Gottschalk for  $Pb(Zr_{0.6}Ti_{0.4})O_3$  [88] and Kolodiaznyi for  $Ba_3MgNb_2O_9$  [98] materials, who obtained 193psec and 205psec, respectively, it is possible to tell that they observed bulk lifetime values (but not average values of several unresolved lifetime components) for the given materials. By substituting two cations on the B-sublattice one would significantly increase the bulk lifetimes from 120-150psec up to approximately 190-240psec.

## 6.2.2 $Ba_{3+3x}CoNb_2O_9$ Samples

The dependence of the bulk lifetime on the fractional part of barium in  $Ba_{3+3x}CoNb_2O_9$  samples is provided in fig.6.9. The bulk lifetime changes from 190psec to 204psec within the studied range of x. By looking on the results of microwave measurements (section 4.2.2) one can see that the dependence of  $\tau_b$  on x is similar to that of the quality factor indicating correlation of these two values.

The X-ray results of the Ukrainian group revealed the presence of  $Ba_6CoNb_9O_{30}$  and small ordering for some nonstoichiometric compositions of  $Ba_3CoNb_2O_9$ . Unfortunately, the sensitivity of the X-ray setup used in these studies did not allow to confirm the presence of the second phase. So, X-ray spectra collected at McMaster University were used to estimate the concentration of cubic and hexagonal phases in nonstoichiometric samples and to obtain lattice parameters for further calculations.

The experimental X-ray spectrum is provided in fig.6.10 giving the following lattice parameters:

-cubic phase  $a=b=c=4.0886\text{\AA}$

The relative concentrations of cubic and hexagonal phases are 97% and 3% for the  $Ba_{0.98}Co_{1/3}Nb_{2/3}O_3$  sample. To the best of our knowledge there are no refined

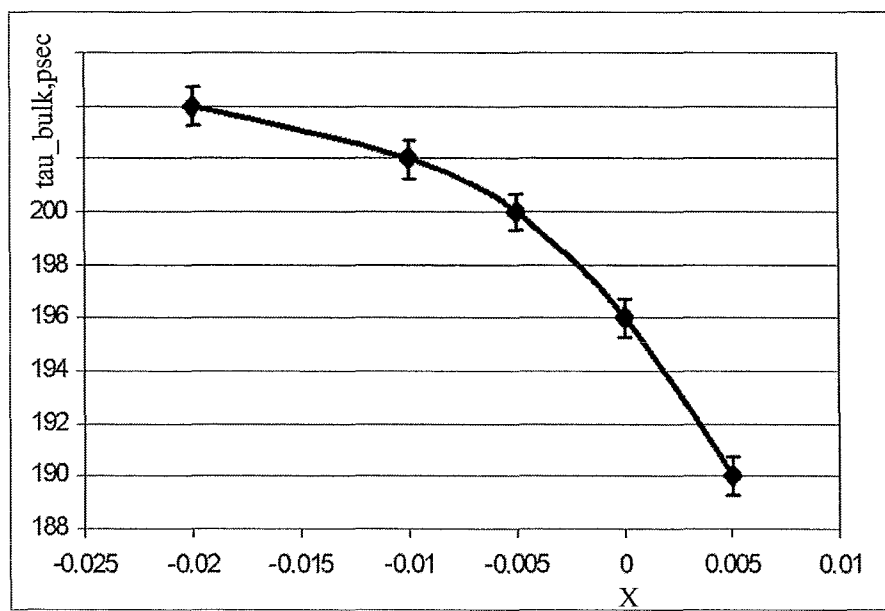


Fig.6.9 Dependence of  $\tau_b$  on the  $1+x$  value for  $Ba_{3+3x}CoNb_2O_9$

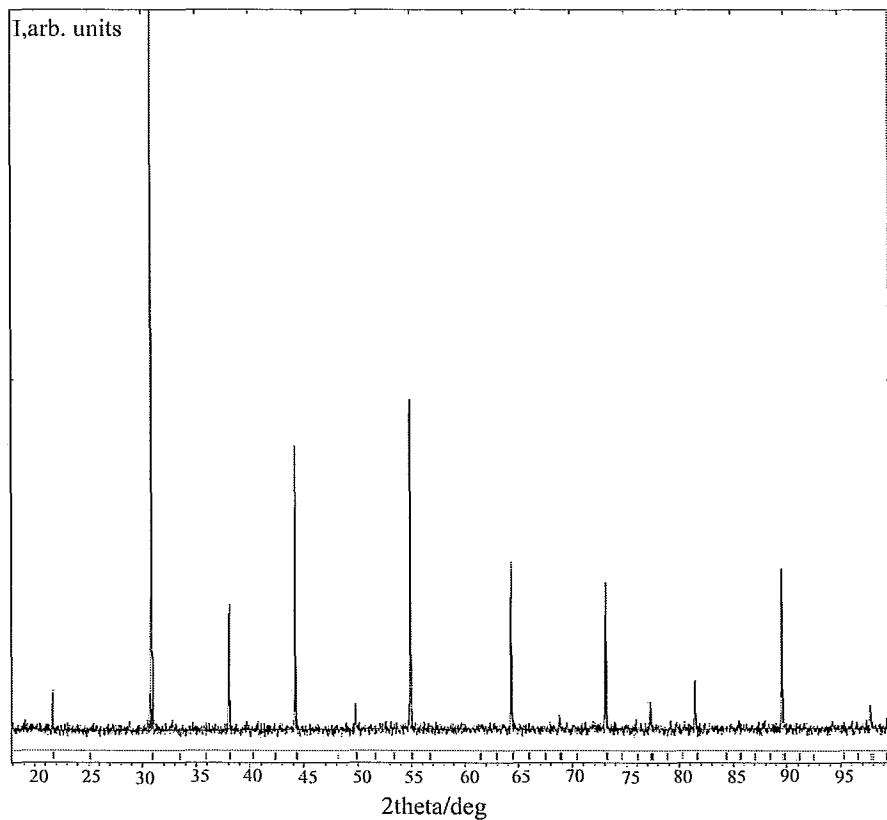


Fig.6.10 X-ray diffraction spectrum for a cobalt niobium perovskite sample

X-ray data available for the hexagonal phase of BCN perovskite. So, only the lifetime for the cubic phase can be calculated theoretically. However, because of the similarity between BMN and BCN systems, the bulk lifetime for the hexagonal phase of cobalt perovskite should be somewhere close to 237psec.

Theoretical simulations for the bulk lifetime in cubic cobalt perovskite resulted in a value of 193.5psec. This is very close to that in the magnesium perovskite system. Regarding the value of the bulk lifetime in the  $Ba_6CoNb_9O_{30}$  phase present in the nonstoichiometric cobalt perovskite, calculations led to  $\tau_b = 353.5\text{ psec}$  (lattice parameters and the symmetry of the system used for calculation were taken from ref.[99]).

For  $1+x=0.98$  and  $0.99$ , the Ukrainian group detected changes in the degree of ordering and concentration of the second phase, both of which decrease by moving toward stoichiometric composition ( $1+x=1$ ).

If one supposes that the contribution from the cation ordering to the bulk lifetime for  $1+x=0.98$  is about 1-2psec (since the concentration of the hexagonal phase is only several percent) the rest originates from the difference in the lifetimes of the host material and  $Ba_6CoNb_9O_{30}$ . From this, the concentration of  $Ba_6CoNb_9O_{30}$  is around 5% for  $1+x=0.98$  and smoothly decreases with  $1+x \rightarrow 1.05$ .

So, changes in the bulk lifetime in  $Ba_{3+3x}CoNb_2O_9$  samples are the result of two competing processes. Since the lifetime of  $Ba_6CoNb_9O_{30}$  (353psec) is much longer than the value of the lifetime for the hexagonal phase of cobalt perovskite (around 237psec), the former more significantly influences the positron results. Thus,

it is possible to trace the change in the concentration of the second phase, which should completely disappear in the  $Ba_{1.05}Co_{1/3}Nb_{2/3}O_3$  sample.

### 6.2.3 $Ba_3Co_{1+x}Nb_2O_9$ Samples

By comparing Table 4.1 (on page 51, containing results of X-ray and microwave measurements) with the microwave data for the quality factor and fig.6.11, containing results of positron lifetime spectroscopy ( $\tau_b$ ) one can notice the same trend in the change of both values with x. However, contrary to  $Ba_{3+3x}CoNb_2O_9$  samples, in which the  $Ba_6CoNb_9O_{30}$  phase degraded the quality factor and simultaneously increased the bulk lifetime, the presence of the second phase in  $Ba_3Co_{1+x}Nb_2O_9$  decreases the Q-factor as well as  $\tau_b$ .

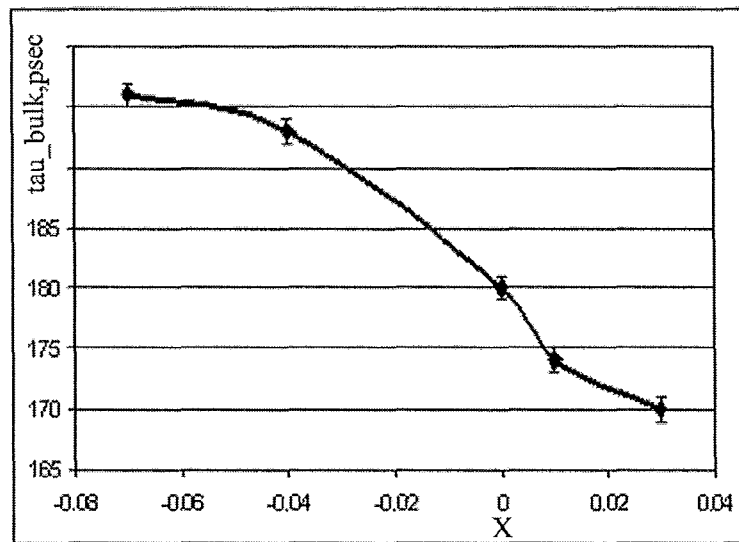


Fig.6.11 Dependence of  $\tau_b$  on  $l+x$  value for  $Ba_3Co_{1+x}Nb_2O_9$

As was mentioned in the previous section the theoretical bulk lifetime for the BCN perovskite is 193.5psec. From this, only  $Ba_3Co_{0.96}Nb_2O_9$  can be considered as a single phase ceramic for which  $\tau_b = 196\text{ p sec}$ . According to the results of X-ray measurements conducted by the Ukrainian group,  $Ba_3Co_{0.93}Nb_2O_9$  contains small traces of  $Ba_5Nb_4O_{15}$ , which disappear with increasing  $1+x$  value. Theoretical simulations on the bulk lifetime in  $Ba_5Nb_4O_{15}$  material (lattice data were taken from reference [100]) resulted in  $\tau_b = 426.6\text{ p sec}$ . This means that  $Ba_3Co_{0.93}Nb_2O_9$ , whose  $\tau_b = 196\text{ p sec}$  contains roughly 0.5% of  $Ba_5Nb_4O_{15}$ .

The further decrease of the bulk lifetime with increasing  $1+x$  value is caused by the presence of some other second phase. Different barium rich materials that were studied by X-ray diffraction exhibit reduced electron density which should result in longer lifetime values in comparison with cubic  $Ba_3CoNb_2O_9$  perovskites. So, drastic decreases in the bulk value (more than 20psec from the cubic phase perovskite) could not be explained by the presence of barium rich material. Only material with pretty high electron density could lead to a decrease of the bulk lifetime of cobalt perovskite and the concentration of this material is so small that the X-ray technique is not sensitive enough to reveal it.

According to the literature data, cobalt rich substances have an electronically compact structure. For example, cobalt oxide [101] has lattice constants  $a=b=c=2.997\text{\AA}$ , which are much smaller than those for cubic cobalt perovskite ( $a=b=c=4.0886\text{\AA}$ ). Because of the large difference in the lattice parameters of these two materials, one possibly can expect the bulk lifetime for cobalt oxide to be around 120-150psec. In this case, increasing the concentration of cobalt oxide

(when  $1+x \rightarrow 1.03$ ) would decrease the value of the bulk lifetime for the whole system.

So, the positron lifetime technique possesses higher sensitivity to the presence of the second phases in the host material when the bulk lifetimes of the main material and impurities are different. Although positron lifetime spectroscopy does not allow unambiguous detection of the second phases, it can give directions for further clarification by some other techniques.

#### **6.2.4 $Ba_{3+3x}ZnNb_2O_9$ vs $Ba_3Zn_{1+x}Nb_2O_9$ Samples**

Changes in the values of the bulk lifetimes in  $Ba_{3+3x}ZnNb_2O_9$  samples (fig.6.12 and fig.6.13) are caused again by the mutual influence of two factors: small B-site cation ordering that should be less for samples annealed at lower temperatures and the presence of second phases, the concentration of which decreases toward compositions close to the stoichiometric ones.

Ukrainian X-ray results demonstrated the possible presence of  $Ba_5Nb_4O_{15}$  and phases analogous to  $Ba_6CoNb_9O_{30}$  ( $Ba_6ZnNb_9O_{30}$ ). The theoretical bulk lifetime of  $Ba_5Nb_4O_{15}$  is 426.6 psec and that of  $Ba_6CoNb_9O_{30}$  353.5 psec. Again, as in the case of the hexagonal phase of magnesium and cobalt perovskites, because of the similarity between  $Ba_6CoNb_9O_{30}$  and  $Ba_6ZnNb_9O_{30}$  materials one would expect that the theoretical bulk lifetime of  $Ba_6ZnNb_9O_{30}$  should be near 353 psec. Regarding the host

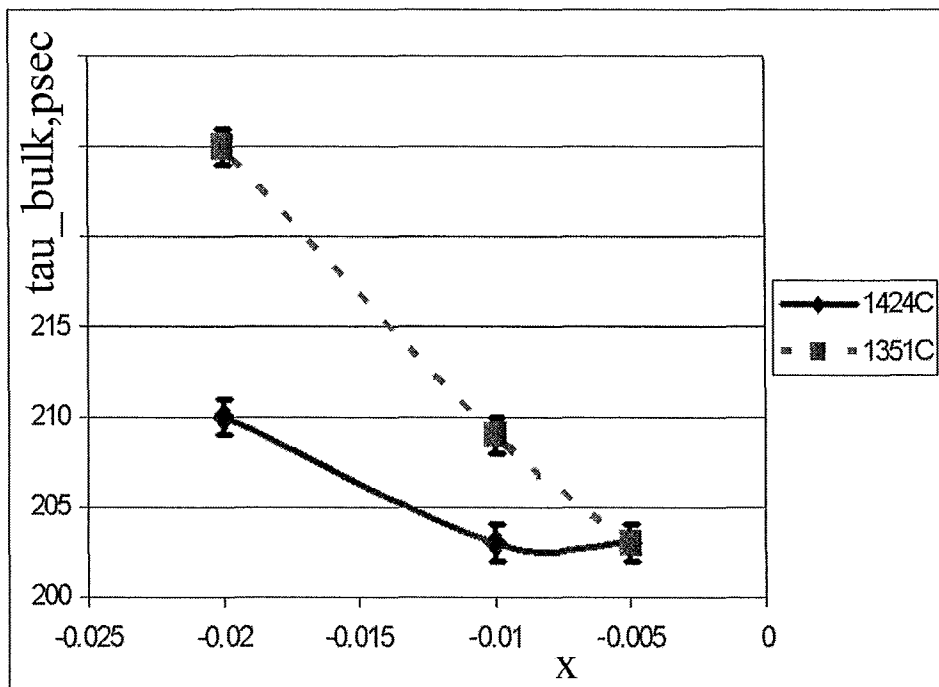


Fig.6.12 Dependence of  $\tau_b$  on  $1+x$  value for  $Ba_{3+3x}ZnNb_2O_9$  perovskite

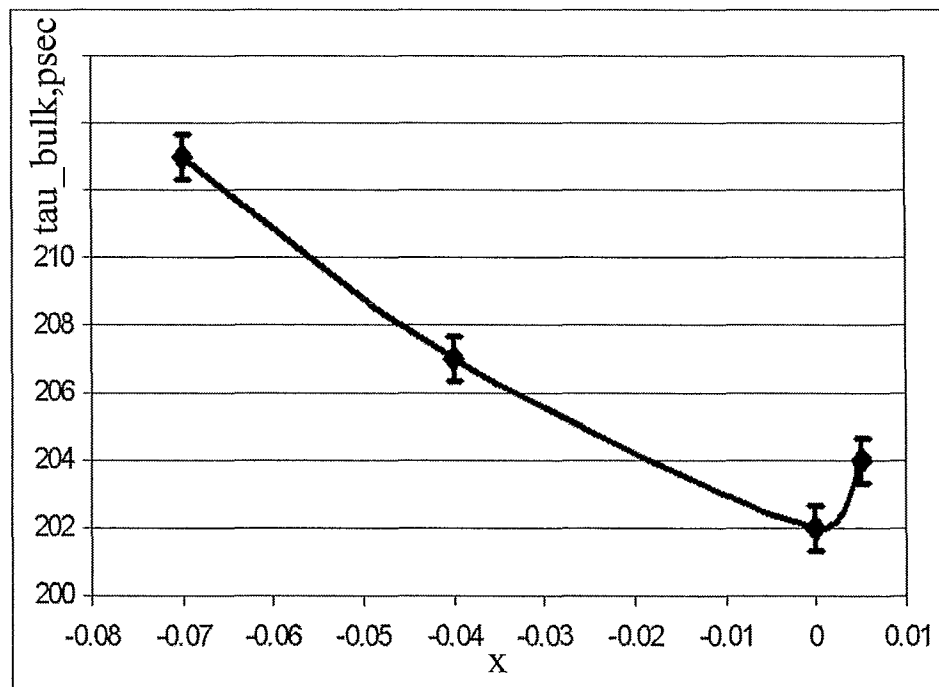


Fig.6.13 Dependence of  $\tau_b$  on  $1+x$  value for  $Ba_3Zn_{1+x}Nb_2O_9$  perovskite

material, simulations of the bulk lifetime in pure cubic zinc perovskite ( $a=b=c=4.0699\text{\AA}$ ) resulted in  $\tau_b = 193\text{ psec}$ .

As in the case of cobalt perovskites, because of the large difference in  $\tau_b$  of the main material and the second phases, the variation in  $\tau_b$  is mostly determined by the changes in concentration of the second phases which decrease when moving toward stoichiometric composition. Samples prepared at slightly higher temperatures ( $1424^\circ\text{C}$ ) demonstrate larger concentrations of the second phases. If one extrapolates the dependence of  $\tau_b$  on  $1+x$  to stoichiometric zinc perovskite (fig.6.12) one would probably obtain a mixture of just cubic and hexagonal zinc perovskite without the presence of any other second phases. In this case, the expected bulk lifetime should be around 195psec.

By changing the zinc concentration in  $Ba_3Zn_{1+x}Nb_2O_9$  samples a similar behaviour in  $\tau_b$  was observed (fig.6.13): at first, the bulk lifetime decreases (indicating decreasing concentrations of the second phases), reaches its minimum for  $BaZn_{1/3}Nb_{2/3}O_3$ , and then increases again indicating the appearance of impurities.

## 6.2.5 Defects in Perovskite Materials

Theoretical defect lifetimes in all three perovskite ceramics were calculated within the scheme used for the determination of the bulk lifetime and are presented in Table 6.3. For convenience, the bulk lifetimes reported in the previous sections are also included here.

Table 6.3 Theoretical bulk and defects lifetimes for  $BaA_{1/3}Nb_{2/3}O_3$  (A=Mg,Co or Zn)

	$BaMg_{1/3}Nb_{2/3}O_3$	$BaMg_{1/3}Nb_{2/3}O_3$	$BaCo_{1/3}Nb_{2/3}O_3$	$BaZn_{1/3}Nb_{2/3}O_3$
	cubic	hexagonal	cubic	cubic
$\tau_b$ , psec	194.9	237.1	193.5	192.9
$\tau_{Ba}$ , psec	320.7	-	322.3	320.9
$\tau_A$ , psec	263.9	-	263.5	260.4
$\tau_{Nb}$ , psec	264.5	-	264.7	262
$\tau_O$ , psec	197.3	-	195.4	194.2

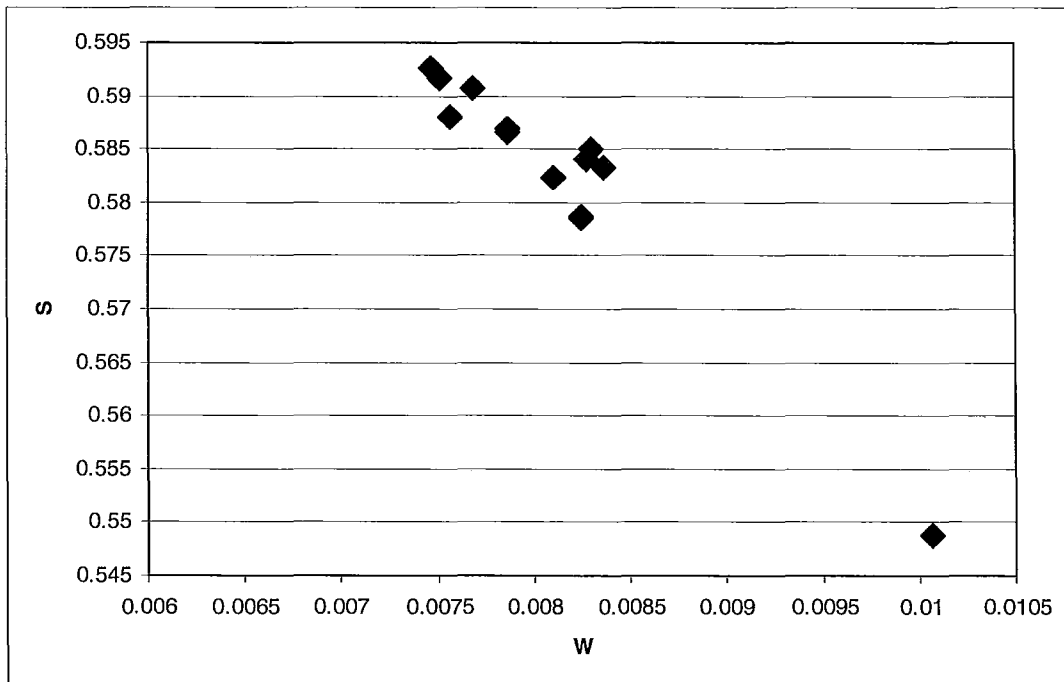


Fig.6.14 S vs W curve for perovskite materials

Lifetimes in the oxygen defects are very close to the bulk values for all three materials indicating an inability for positrons to detect oxygen vacancies, as was the case in the columbite samples. For the barium, niobium and A-vacancies (A=Mg,Co or Zn) the defect lifetime is quite far from the  $\tau_b$  values. This fact favors application of positron lifetime spectroscopy to study the formation of the given defects.

Unfortunately, for the samples used in the current studies, the lifetime component originating from the positrons annihilating in the grain boundaries is around 300psec, which is very close to the lifetimes of Ba, Nb or A-defects. This impeded us from the detection of any of such defects inside of the grains.

To check for the possible presence of defects inside of the bulk of the grains, coincidence Doppler broadening measurements were performed on perovskite type materials and the results are presented in fig. 6.14 as a S-W curve. The S *versus* W dependence is linear, indicating the presence of just one type of defects: grain boundaries.

## **Chapter 7 Conclusions and Suggestions for Future Work**

Defect structure of  $Ba_3ANb_2O_9$  (A=Mg,Co or Zn) perovskites as well as  $ANb_2O_6$  (A=Mg,Co or Zn) columbites used as a precursor was studied by means of positron annihilation spectroscopy. Positron lifetime spectroscopy revealed presence of the grain boundaries the size of which varies within studied columbite samples. Conducted theoretical simulations of the bulk lifetime for columbites are in an agreement with the experimental values and were around 170psec.

Deviation from stoichiometry results in the appearance of second phases in the perovskite type materials the change in the concentration of which can be observed by positron lifetime spectroscopy. It was shown theoretically that positrons are sensitive to the ordering in  $Ba_3ANb_2O_9$  perovskites. On practice, however, because of the presence of second phases with the bulk lifetimes significantly longer than those for the perovskites, it was not possible to observe ordering in the perovskite systems.

Present work concentrated on application of Positron Annihilation Spectroscopy to study defects' structure in perovskite materials having two types of cation atoms on B-sublattice. It was demonstrated that addition of the second cation significantly changes positron characteristics in the bulk of material. Because of limited number of publications on the application of Positron Spectroscopy to the perovskite ceramics it would be interesting to more closely investigate this tendency for other perovskite materials with one and two cations on B-site.

Reflection microscopy measurements demonstrated "ball-like" particles inside of perovskite samples. Defect lifetimes that arise because of the annihilation in the grain boundaries of perovskites depend on the shape of the grains and were around

300psec. The choice of samples used in present studies did not allow us to look on influence of particles' shape on the lifetime inside of the grain boundaries which should be different for "needle-like" particles. Sharp edges can induce electric field between grains that influence both microwave and positron characteristics of material.

One of the requirements to the ceramics that can be used in microwave applications is near zero temperature coefficient of resonant frequency. Magnesium, zinc and cobalt perovskites used in present work have TCF far from zero. By mixing, for example, magnesium and cobalt perovskites, TCF can be tuned to acceptable value. Because of absence of literature data on the positron results for that and similar system, Positron Annihilation Spectroscopy still has wide and fruitful field to study defects complex systems like  $Ba_3(Zn_{1-y}Co_y)Nb_2O_9$  with their further correlation with microwave measurements.

## References

- 1 W. Wersing, High frequency ceramic dielectrics and their application for microwave components. Electronic Ceramics. Edited by Steele BCH. London and New York: Elsevier Applied Science; 67 (1991)
- 2 W. Wersing, Current Opinion in Solid State and Materials Science, 1, 715 (1996)
- 3 A.J. Moulson and A.J. Herbert, Electroceramics (Chapman and Hall, London, 1990)
- 4 T. Kolodiaznyi, PhD Thesis, McMaster University (2002)
- 5 C.C. Lee and P. Lin, Jpn. J. Appl. Phys., 37, 878 (1998)
- 6 J.J. Wu and X.M. Chen, J. Europ. Ceram. Soc., 19, 1123 (1999)
- 7 A.G. Belous and O.V. Ovchar, J. Europ. Ceram. Soc., 19, 1119 (1999)
- 8 M. Onoda, J. Kuwata, K. Kaneta, K. Toyama, and S. Nomura, Jpn. J. Appl. Phys., 21, 1707 (1982)
- 9 H. Banno, F. Mizuno, T. Takeuchi, T. Tsunooka, and K. Ohya, Jpn. J. Appl. Phys., 21 Supplement 24-3, 87 (1985)
- 10 H. Tamura, T. Konoike., Y. Sakabe, and K. Wakino, J. Am. Ceram. Soc., 67, C-59 (1984)
- 11 M. Valant, D. Suvorov, C. Hoffmann, and H. Sommariva, J. Europ. Ceram. Soc., 21, 2647 (2001)
- 12 H.M. O'Bryan, J. Thompson, and J.K. Plourde, J. Am. Ceram. Soc., 57, 450 (1974)

- 13 J.K. Plourde, D.F. Linn, H.M. O'Bryan, J. Thompson, *J. Am. Ceram. Soc.*, 58,  
418 (1975)
- 14 T. Negas., G. Yeager, S. Bell, N. Coats, and I. Minis, *Am. Ceram. Soc. Bull.*,  
72, 80 (1993)
- 15 R.J. Cava, *J. Mater. Chem.*, 11, 54 (2001)
- 16 P.K. Davies, J. Tong, and T. Negas, *J. Am. Ceram. Soc.*, 80, 1727 (1997)
- 17 R.E. Newnham, *J. Am. Ceram. Soc.*, 50, 216 (1967)
- 18 A.E. McHale, R.S. Roth, *J. Am. Ceram. Soc.*, 69, 827 (1986)
- 19 F. Azough, PhD Thesis, University of Manchester (1991)
- 20 R. Christoffersen, P.K. Davies, X. Wei, and T. Negas, *J. Am. Ceram. Soc.*, 77,  
1441 (1994)
- 21 D. Kolar, Z. Stadler, S. Gaberscek, D. Suvorov, *Ber. Deut. Keram. Ges.*, 55,  
346 (1978)
- 22 S. Nomura, K. Toyama, and K. Kaneta, *Jpn. J. Appl. Phys.*, 21, L684 (1982)
- 23 H. Matsumoto, H. Tamura, and K. Wakino, *Jpn. J. Appl. Phys.*, 30, 2347  
(1991)
- 24 S.B. Desu and H.M. O'Bryan, *J. Am. Ceram. Soc.*, 68, 546 (1985)
- 25 A. Dias and R.L. Moreira, *J. Appl. Phys.*, 94, 3414 (2003)
- 26 K. Fukuda and R. Kitoh, *J. Am. Ceram. Soc.*, 77, 149 (1994)
- 27 T. Nagai, M. Sugiyama, M. Sando, and K. Niihara, *Jpn. J. Appl. Phys.*,  
36(3A), 1146 (1997)
- 28 L. Chai and P. Davies, *J. Am. Ceram. Soc.*, 80, 3193 (1997)
- 29 H. Tamura, D.A. Sagala, and K. Wakino, *Jpn. J. Appl. Phys.*, 25, 787 (1986)

- 30 H. Tamura, Jpn. J. Appl. Phys, 32(6A), 2774 (1993)
- 31 T. Takahashi, Jpn. J. Appl. Phys, 39, 5637 (2000)
- 32 P.K. Davies and J. Tong, J. Am. Ceram. Soc., 80, 1727 (1997)
- 33 F. Galasso and J. Pyle, Inorganic Chemistry, 2, 482 (1963)
- 34 A.J. Jacobson, B.M. Collins, and B.E.F. Fender, Acta Crystallogr., B32, 1083 (1976)
- 35 S. Kawashima, M. Nishida, J. Ueda, and H. Ouchi, J. Am. Ceram. Soc., 66, 421 (1983)
- 36 K. Matsumoto, T. Hiuga, K. Takada, and H. Ichimura, pp.118-21, In Proceedings of the 6<sup>th</sup> IEEE International Symposium on Application of Ferroelectrics (June 1986). Institute of Electrical and Electronic Engineers, New York 1986.
- 37 I.T. Kim, T.S. Oh, and Y.H. Kim, J. Mater. Sci. Lett., 12, 182 (1993)
- 38 I.M. Reaney, E.L. Colla, and N. Setter, Jpn. J. Appl. Phys, 33, 3984 (1994)
- 39 E.L. Colla, I.M. Reaney, and N. Setter, Ferroelectrics, 133, 217 (1992)
- 40 E. Colla, I.M. Reaney, and N. Setter, J. Appl. Phys., 74, 3414 (1993)
- 41 H.D. Megaw, Proc. Phys. Soc., 58, 133 (1946)
- 42 H.D. Megaw, Crystal structures: A Working Approach (W.B. Saunders Company, London, 1973), p.273
- 43 O. Muller and R. Roy, The Major Ternary Structural Families (Springer Verlag, Berlin, 1974)
- 44 S.J. Penn, N. Alford, A. Templeton, X. Wang, M. Xu, M. Reece, and K. Schrapel, J. Am. Ceram. Soc., 80, 1885 (1997)

- 45 A. Templeton, X. Wang, S.J. Penn, S.J. Webb, L.F. Cohen, and N. Alford, J.  
Am. Ceram. Soc., 83, 95 (2000)
- 46 S. Nomura, Ferroelectrics, 49, 61 (1983)
- 47 R.I. Scott, M. Thomas, C. Hampson, J. Europ. Ceram. Soc., 23, 2467 (2003)
- 48 I.M. Reaney, Y. Iqbal, H. Zheng, A. Feteira, H. Hughes, D. Iddles, D. Muir,  
T. Price, J. Europ. Ceram. Soc. 25, 1183 (2005)
- 49 Cheol-Woo Ahn, S. Nahm, S.J. Yoon, H.M. Park, and H.J. Lee, Jpn. J. Appl.  
Phys., 42, 6964 (2003)
- 50 H. Hughes, D.M. Iddles, and I.M. Reaney, Appl. Phys. Lett., 79, 2952 (2001)
- 51 S. Janaswamy, G.S. Murthy, E.D. Dias, and V.R.K. Murthy, Mater. Lett., 55,  
414 (2002)
- 52 J. Joseph, Dias, T.M. Vimala, V.R.K. Murthy, Jpn. J. Appl. Phys., 41, 3010  
(2002)
- 53 Dmowski, M.K. Akbas, P.K. Davies, and T. Egami, J. Phys. Chem. Solids, 61,  
229 (2000)
- 54 R.L. Moreira, F.M. Matinaga, and A. Dias, Appl. Phys. Lett., 78, 428 (2001)
- 55 R. Behringer and C.G. Montgomery, Phys. Rev., 61, 222 (1942)
- 56 R. Krause-Rehberg and H.S. Leipner, “Positron Annihilation in  
Semiconductors”, (1999)
- 57 M.J. Puska, R.M. Nieminen, Rev. Modern Phys., 66, 841 (1994)
- 58 P. Asoka-Kumar, K.G. Lynn, and D.O. Welch, J. Appl. Phys., 76, 4935  
(1994)
- 59 A. Perkins and J.P. Carbotte, Phys. Rev. B, 1, 101 (1970)

- 60 R.M. Nieminen and J. Oliva, Phys. Rev. B, 22, 2226 (1980)
- 61 W. Brandt and R. Paulin, Phys. Rev. B, 15, 2511 (1977)
- 62 M. Mourino, H. Lobl, and R. Paulin, Phys. Lett., 71A, 106 (1979)
- 63 M. Bertolaccini, A. Dupasquier, Phys. Rev. B, 1, 2896 (1970)
- 64 P.A. Sterne and J.H. Kaiser, Phys. Rev. B, 43, 13892 (1991)
- 65 E. Boronski and R.M. Nieminen, Phys. Rev. B, 34, 3820 (1986)
- 66 I. Makkonen, M. Hakala, and M.J. Puska, Phys. Rev. B, 73, 35103 (2006)
- 67 B. Barbiellini, M.J. Puska, T. Korhonen, A. Harju, T. Torsti, and R.M. Nieminen, Phys. Rev. B, 53, 16201 (1996)
- 68 B. Barbiellini, M.J. Puska, T. Torsti, and R.M. Nieminen, Phys. Rev. B, 51, R7341 (1995)
- 69 P.A. Sterne and J.H. Kaiser, Phys. Rev. B, 43, 13892 (1991)
- 70 J.P. Perdew, Physica B, 172, 1 (1991)
- 71 J.P. Perdew, In Electronic Structure of Solids '91, edited by P. Ziesche and H. Eschrig (Akademie Verlag, Berlin, 1991)
- 72 J.P. Perdew, J.A. Chevary, S.H. Vosko, K.A. Jackson, M.R. Pederson, D.J. Singh, and C. Fiolhais, Phys. Rev. B, 46, 66 (1971)
- 73 G. Ortiz and P. Ballone, Phys. Rev. B, 43, 6376 (1991)
- 74 J.P. Perdew, J.A. Chevary, S.H. Vosko, K.A. Jackson, M.R. Pederson, D.J. Singh, and C. Fiolhais, Phys. Rev. B, 48, 4978(E) (1993)
- 75 L. Lantto, Phys. Rev. B, 36, 5160 (1987)
- 76 J. Arponen and E. Pajanne, Ann. Phys., 121, 343 (1979)
- 77 C.H. Leung, M.J. Stott, and C.O. Ambladh, Phys. Lett., 57A, 26 (1976)

- 78 H. Stachowiak and J. Lach, Phys. Rev. B, 48, 9828 (1993)
- 79 S. Szpala, P. Aspka-Kumar, B. Nielsen, J.P. Peng, S. Hayakawa, and K.G. Lynn, Phys. Rev. B, 54, 4722 (1996)
- 80 A. Harrich, S. Jagsch, S. Riedler, and W. Rosinger, Am. J. Undergrad. Research, 2, 13 (2003)
- 81 P. Asoka-Kumar, M. Alatalo, V.J. Ghosh, A.C. Kruseman, B. Nielsen, and K.G. Lynn, Phys. Rev. Lett., 77, 2097 (1996)
- 82 K.G. Lynn and A.N. Goland, Solid State Commun., 18, 1549 (1976)
- 83 V.J. Ghosh and B. Nielsen, Phys. Rev. B, 61, 207 (2000)
- 84 E.C. Subbarao and G. Shirane, J. Am. Ceram. Soc., 42, 279 (1959)
- 85 D. Hennings and K.H. Hardtl, Phys. Status Soliditi A, 8, 465 (1970)
- 86 T. Friessneg, S. Madhukar, B. Nielsen, A.R. Moodenbaugh, S. Aggarwal, D.J. Keeble, E.H. Poindexter, P. Mascher, and R. Ramesh, Phys. Rev. B, 59, 13365 (1999)
- 87 K. Suvegh, A. Domjan, R. Tarsoly, and A. Vertes, J. Radioanal. Nucl. Chem. 211, 255 (1996)
- 88 S. Gottschalk, H. Hahn, A.G. Balogh, W. Puff, H. Kungi, and M.J. Hoffmann, J. Appl. Phys., 96, 7464 (2004)
- 89 D.J. Keeble, S. McGuire, S. Singh, B. Su, T.W. Button, and J. Petzelt, J. Phys., 128, 111 (2005)
- 90 C. Hubner, T. Staab, and R. Krause-Rehberg, Appl. Phys. A, 61, 203 (1995)
- 91 A. Belous, O. Ovchar, B. Jancar, J. Bezjak, G. Annino, D. Grebennikov, and P. Mascher, to be published

- 92 P. Kirkegaard, N.J. Pedersen, M. Eldrup, PATFIT-88 : a data-processing system for positron annihilation spectra on mainframe and personal computers, Risø National Laboratory, Denmark (1989)
- 93 T. Torsti, M. Heiskanen, M. J. Puska and R. M. Nieminen, MIKA: a multigrid-based program package for electronic structure calculations
- 94 S. Pagola, R.E. Carbonio, J.A. Alonso, and M.T. Fernandez-Diaz, J. Solid State Chem. 134, 76 (1997)
- 95 M. Waburg, and H. Mueller-Buschbaum, Zeitschrift fuer Anorganische und Allgemeine Chemie 508, 55 (1984)
- 96 H. Weitzel, Zeitschrift fuer Kristallographie, Kristallphysik, Kristallchemie 144, 238 (1977)
- 97 N. Kumada, K. Taki, N. Kinomura, Mater. Research Bulletin, 35, 1017 (2000)
- 98 T. Kolodiaznyi, G. Annino, A. Younker, P. Malysz, P. Mascher, H. Haneda, J. Europ. Ceram. Soc., 26, 1921 (2006)
- 99 U. Lehmann and H. Mueller-Buschbaum, Zeitschrift fuer Anorganische und Allgemeine Chemie, 481, 7 (1981)
- 100 S. Pagola, G. Polla, G. Leyva, M.T. Casais, J.A. Alonso, I. Rasines, R.E. Carbonio, Mater. Sci. Forum, 228, 819 (1996)
- 101 S. Saito, K. Nakahigashi, and Y. Shinomura, J. Phys. Soc. Jpn., 21, 850 (1966)